MOUSE EMBRYONIC STEM CELLS REQUIRE SUSTAINED DNMT1-MEDIATED DNA METHYLATION MAINTENANCE FOR EPIGENOMIC, GENOMIC AND FUNCTIONAL INTEGRITY

Elizabeth Elder[1,2], Anthony Lemieux[1,2], Lisa-Marie Legault[1,2], Maxime Caron[3], Virginie Bertrand-Lehouillier[1,2], Thomas Dupas[1,2], Noël Raynal[2,4], Guillaume Bourque[5,6], Daniel Sinnett[2,7], Nicolas Gévry[8], Serge McGraw[1,2,9,10]

[1] Department of Biochemistry and Molecular Medicine, University of Montreal, Montreal, Quebec, Canada
[2] Azrieli Research Center of Sainte-Justine University Hospital, Montreal, Quebec, Canada
[3] University of Montreal Hospital Centre, Montreal, Quebec, Canada
[4] Department of Pharmacology and Physiology, University of Montreal, Montreal, Quebec, Canada
[5] Department of Human Genetics, McGill University, Montreal, Quebec, Canada
[6] McGill Genome Centre, Montreal, Quebec, Canada
[7] Department of Pediatrics, University of Montreal, Montreal, Quebec, Canada
[8] Department of Biology, University of Sherbrooke, Sherbrooke, Quebec, Canada
[9] Department of Obstetrics and Gynecology, University of Montreal, Montreal, Quebec, Canada
[10] Lead contact, correspondence: serge.mcgraw@umontreal.ca

SUMMARY

Our research is motivated by the pivotal role of DNMT1 in maintaining DNA methylation, genomic stability, transposable element silencing, and imprinting alongside the extensive utilization of embryonic stem cells (ESCs) for modeling development and disease. Previously, we showed that DNA hypomethylation persisted throughout *Dnmt1* inactivation and rescue in mouse ESCs (mESCs), demonstrating their need for sustained DNMT1 activity. Here, expanding on our previous work, we assessed the broader epigenomic impact using EM-seq for enhanced DNA methylation coverage and sensitivity, ChIP-seq for five histone modifications and differential gene expression analysis, revealing dynamic epigenomic remodeling. We uncovered 20 regions with imprinted-like signatures and observed permanent de-repression of MERVL and MT2 transposable elements potentially associated with gene transcript chimerism. Genomic instability, cellular dysfunction, and lasting effects upon differentiation into germ layer lineages were also detected. Our findings enlighten DNMT1-dependent mechanisms in mESCs, offering foundational insights into developmental biology, disease pathogenesis and regenerative medicine.

KEYWORDS

Epigenetics, Embryonic stem cells, DNMT1, DNA methylation, Histone modifications, Gene expression regulation, Genomic instability, Genomic imprinting, Transposable elements, Cellular differentiation

HIGHLIGHTS

- Epigenomic stress induced by *Dnmt1* inactivation in mESCs persists after *Dnmt1* rescue
- Identification of 20 regions with imprinted-like epigenetic and regulatory signatures
- MERVL and MT2 LTR de-repression with evidence of related gene transcript chimerism
- Genomic instability, cellular dysfunction, and lasting effects upon differentiation

GRAPHICAL ABSTRACT

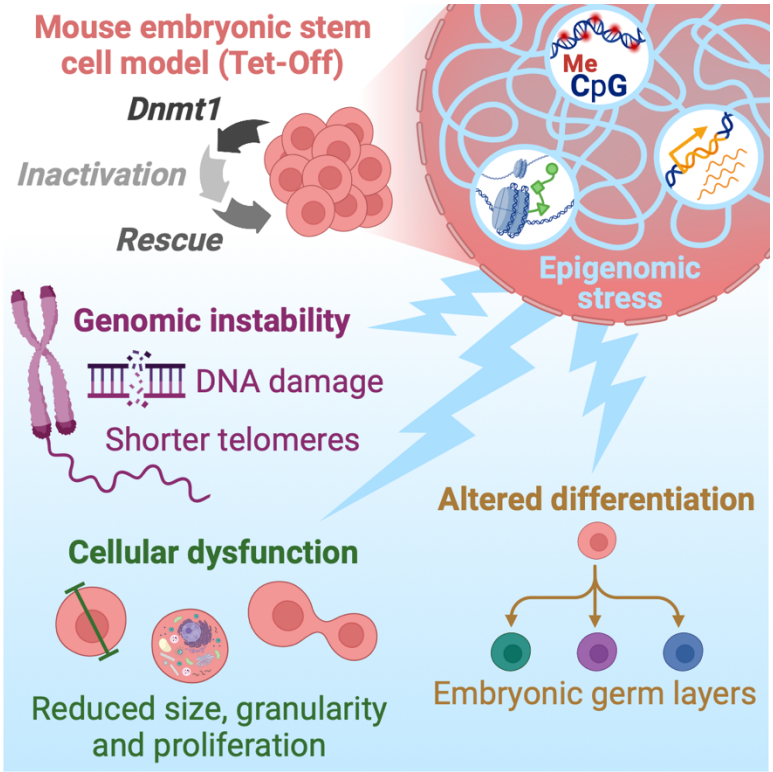

INTRODUCTION

Epigenetic mechanisms, including DNA methylation and histone modifications, regulate chromatin structure, gene expression and cellular processes in response to developmental cues, environmental stimuli, and cellular stressors, without alterations to the underlying DNA sequence[1-4]. Within this intricate framework, pluripotent embryonic stem cells (ESCs) are quintessential models for deciphering the interplay between epigenetics and cellular identity[5-7].

DNA methyltransferase 1 (DNMT1) stands as a pivotal guardian of epigenetic information by ensuring faithful maintenance of DNA methylation during cell division[8-11], a process particularly intensified in the highly proliferative context of ESCs. By methylating cytosine residues primarily at CpG dinucleotides (i.e. CpG methylation), DNMT1 is involved in safeguarding genomic stability[12], transposable element silencing[13] and gene expression regulation[14]. *Dnmt1* knock-out is lethal in mouse embryos[15] and leads to extensive DNA hypomethylation in human[16] and mouse[17] ESCs (mESCs). Moreover, DNMT1 extends its influence on epigenetic regulation by interacting with histone modifiers[18], chromatin remodelers[19] and non-coding RNAs[20]. DNMT1 thus has a fundamental role in orchestrating cell fate decisions and lineage commitments[21-23], for which ESCs serve as excellent model systems. Dysregulation of DNMT1 activity has profound implications for cellular homeostasis, contributing to pathogenesis of various diseases including cancer[24], developmental disorders[25], and adult-onset neurodegenerative pathologies[26,27]. Unravelling the molecular and cellular mechanisms governed by DNMT1-mediated epigenetic regulation in ESCs can offer valuable insights into developmental and pathological processes as well as provide foundational knowledge for future advancements in stem cell-based regenerative medicine.

In developmental biology, an important aspect of DNMT1 function is its role in genomic imprinting[28-30], an epigenetic phenomenon whereby certain genes exhibit parent-of-origin-specific expression[31]. These imprinted genes are controlled by imprinting control regions (ICRs) and germline differentially methylated regions (gDMRs) which acquire oocyte- or sperm-specific DNA methylation patterns during gametogenesis. In offspring, this results in allele-specific DNA methylation at ICRs and gDMRs, dictating the monoallelic expression of imprinted genes. Imprinted DNA methylation must be maintained throughout embryonic development and postnatally by the concerted actions of DNMT1 and other regulatory factors, such as ZFP57, TRIM28 and SETDB1-mediated H3K9me3 deposition[32-35]. Failure of imprinted DNA methylation maintenance can lead to severe imprinting-related developmental disorders[36,37].

Our prior research revealed that CpG hypomethylation induced by *Dnmt1* inactivation in mESCs persisted post-*Dnmt1* rescue, impacting ICRs and gDMRs with great severity, but also affecting other genomic elements like promoters, gene bodies and repetitive elements[30]. Here, we characterized the broader epigenomic impact of *Dnmt1* inactivation and rescue in mESCs by profiling CpG methylation with enhanced coverage and sensitivity, five key histone modifications (H3K4me3, H3K27ac, H3K4me1, H3K27me3, H3K9me3) and gene expression, all of which exhibited dynamic remodelling. This was accompanied by genomic instability, dysfunction of cellular processes and lasting effects on gene expression patterns upon differentiation to germ layers, underscoring the crucial requirement of sustained DNMT1 activity in mESCs.

RESULTS

Inactivation and rescue of *Dnmt1* in mESCs induces dynamic epigenomic remodelling

Utilizing Tet-Off *Dnmt1* (*Dnmt1*$^{tet/tet}$) mESCs[29], we previously revealed through reduced-representation bisulfite sequencing (RRBS) that loss of CpG methylation due to *Dnmt1* inactivation is not fully restored upon *Dnmt1* rescue[30]. Here, to gain a more comprehensive understanding of the epigenomic repercussions, we employed the same *Dnmt1*$^{tet/tet}$ mESC model and performed enzymatic methyl sequencing (EM-seq), which offered superior CpG coverage and methylation sensitivity compared to RRBS (EM-seq: 15,349,152 sequenced CpGs; RRBS: 1,422,634 sequenced CpGs). We also conducted chromatin immunoprecipitation sequencing (ChIP-seq) for five key histone modifications (permissive: H3K4me3, H3K27ac and H3K4me1; repressive: H3K27me3 and H3K9me3). Herein, untreated *Dnmt1*$^{tet/tet}$ mESCs are referred to as *Dnmt1* control (*Dnmt1*^{CTL}), those after *Dnmt1* inactivation by doxycycline as *Dnmt1* inactive (*Dnmt1*^{INV}), and those after rescuing *Dnmt1* through doxycycline removal as *Dnmt1* rescue (*Dnmt1*^{RES}) (Figure 1A).

We first compared overall methylation levels of single CpGs in *Dnmt1*^{CTL}, *Dnmt1*^{INV}, and *Dnmt1*^{RES} conditions across various genomic location contexts, revealing a near-total depletion in *Dnmt1*^{INV} and a sustained decrease in *Dnmt1*^{RES} for all contexts (Figure 1B). Permanent reduction in CpG methylation levels observed in *Dnmt1*^{RES} was particularly sizable for chromosome X (-17%), chromosome Y (-32%), ICRs and gDMRs (-27%), intergenic (-13%), open sea (-10%), LINEs (-21%), and LTRs (-13%), in contrast to other genomic location contexts (genome-wide: -9%, autosomes: -9%, promoters: -2%, gene bodies: -6%, CpG islands: -0.6%, CGI shores: -1%, CGI shelves: -4%, CTCF-bound candidate cis-regulatory elements (cCREs): -0.4%, SINEs: -5%). However, considering that CpGs in promoters, CpG islands, and CTCF-bound cCREs were mostly poorly methylated in *Dnmt1*^{CTL} (median level < 7%), the extent of their permanent hypomethylation may not be directly comparable to genomic location contexts with initially highly methylated CpGs.

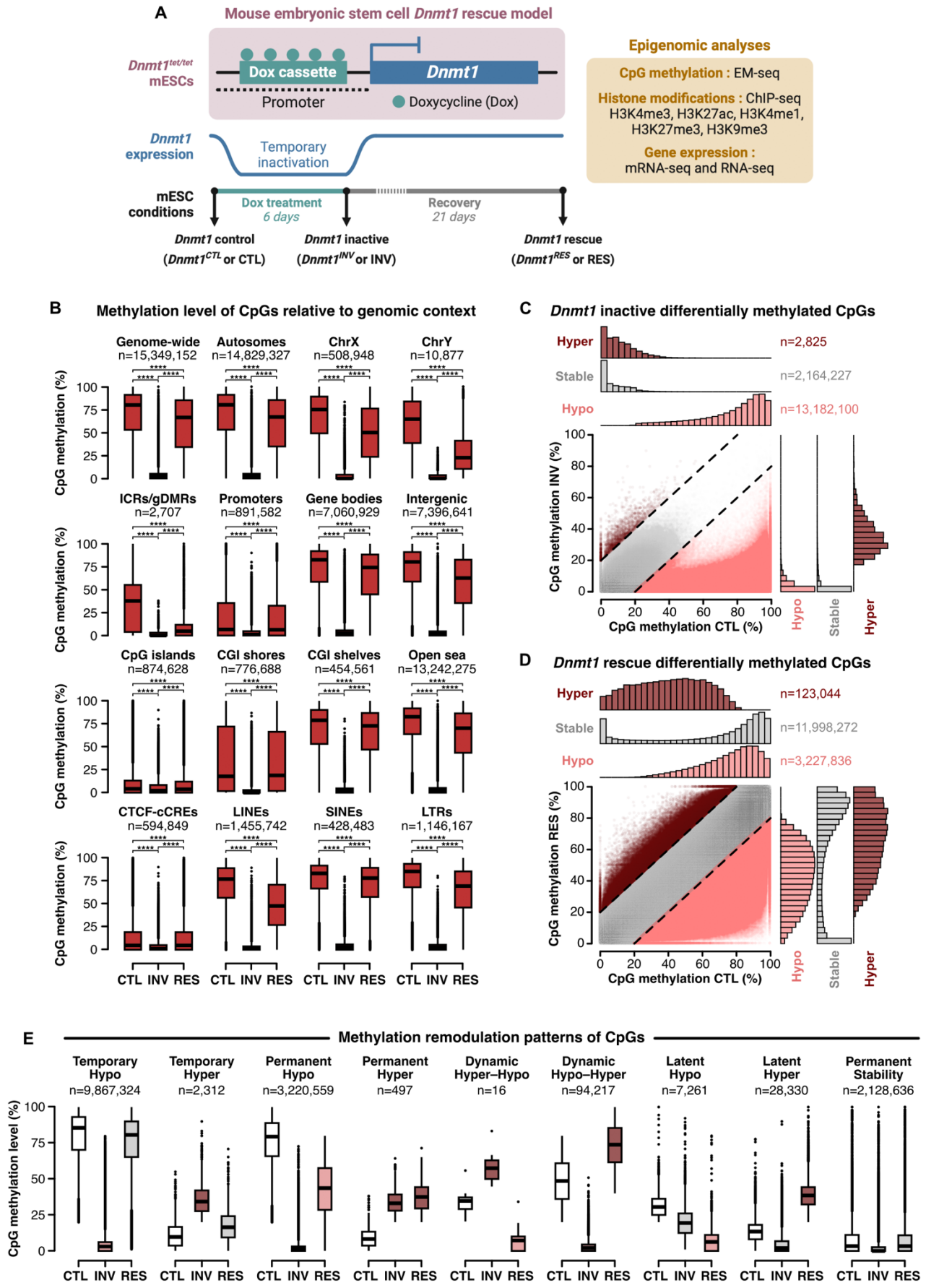
A
Mouse embryonic stem cell Dnmt1 rescue model
Dnmt1tet/tet mESCs
Dox cassette
Dnmt1
Promoter
Doxycycline (Dox)
Dnmt1 expression
Temporary inactivation
mESC conditions
Dox treatment 6 days
Recovery 21 days
Dnmt1 control (Dnmt1CTL or CTL)
Dnmt1 inactive (Dnmt1INV or INV)
Dnmt1 rescue (Dnmt1RES or RES)
Epigenomic analyses
CpG methylation : EM-seq
Histone modifications : ChIP-seq H3K4me3, H3K27ac, H3K4me1, H3K27me3, H3K9me3
Gene expression : mRNA-seq and RNA-seq
B
Methylation level of CpGs relative to genomic context
Genome-wide n=15,349,152
Autosomes n=14,829,327
ChrX n=508,948
ChrY n=10,877
ICRs/gDMRs n=2,707
Promoters n=891,582
Gene bodies n=7,060,929
Intergenic n=7,396,641
CpG islands n=874,628
CGI shores n=776,688
CGI shelves n=454,561
Open sea n=13,242,275
CTCF-cCREs n=594,849
LINEs n=1,455,742
SINEs n=428,483
LTRs n=1,146,167
CpG methylation (%)
CTL INV RES
C
Dnmt1 inactive differentially methylated CpGs
Hyper n=2,825
Stable n=2,164,227
Hypo n=13,182,100
CpG methylation INV (%)
CpG methylation CTL (%)
D
Dnmt1 rescue differentially methylated CpGs
Hyper n=123,044
Stable n=11,998,272
Hypo n=3,227,836
CpG methylation RES (%)
CpG methylation CTL (%)
E
Methylation remodulation patterns of CpGs
Temporary Hypo n=9,867,324
Temporary Hyper n=2,312
Permanent Hypo n=3,220,559
Permanent Hyper n=497
Dynamic Hyper–Hypo n=16
Dynamic Hypo–Hyper n=94,217
Latent Hypo n=7,261
Latent Hyper n=28,330
Permanent Stability n=2,128,636
CpG methylation level (%)
CTL INV RES

Figure 1: *Dnmt1* inactivation and rescue in mESCs permanently reduces CpG methylation levels across various genomic contexts, with over 3.2 million permanently hypomethylated single CpGs. **(A)** Schematic diagram depicting the *Dnmt1*$^{tet/tet}$ mESC model and epigenomic analyses. **(B)** Pairwise comparisons of single CpG methylation levels in *Dnmt1*^{CTL}, *Dnmt1*^{INV} and *Dnmt1*^{RES} relative to genomic context using the Wilcoxon rank sum test with Benjamini-Hochberg p-value adjustment. **(C-D)** Differential methylation of genome-wide single CpGs in *Dnmt1*^{INV} and *Dnmt1*^{RES} versus *Dnmt1*^{CTL}, respectively. Hypermethylation: increase ≥ 20%. Hypomethylation: decrease ≥ 20%. **(E)** Methylation remodulation patterns of single CpGs throughout *Dnmt1* inactivation and rescue determined by their differential state in C and D. Temporary: hypo/hyper in *Dnmt1*^{INV} & stable in *Dnmt1*^{RES}. Permanent: hypo/hyper in both *Dnmt1*^{INV} & *Dnmt1*^{RES}. Dynamic: hypo/hyper in *Dnmt1*^{INV} & the opposite in *Dnmt1*^{RES}. Latent: stable in *Dnmt1*^{INV} & hypo/hyper in *Dnmt1*^{RES}.

To explore genome-wide methylation dynamics of single CpGs throughout *Dnmt1* inactivation and rescue, we measured the change in methylation for each CpG in *Dnmt1*^{INV} versus *Dnmt1*^{CTL} (Figure 1C) and in *Dnmt1*^{RES} versus *Dnmt1*^{CTL} (Figure 1D). A methylation increase ≥ 20% denoted hypermethylated CpGs, while a decrease ≥ 20% indicated hypomethylated CpGs; all others were considered as stable. Each CpG was then categorized based on its methylation change (hypermethylated, hypomethylated, stable) in *Dnmt1*^{INV} and *Dnmt1*^{RES}, revealing nine remodulation patterns (Figure 1E). Among these, temporary hypomethylation, permanent hypomethylation, and permanent stability of methylation were the most prevalent, comprising ~9.9 million, ~3.2 million, and ~2.1 million CpGs, respectively. Although permanent stability was prominent, those CpGs were mostly poorly methylated in *Dnmt1*^{CTL} (median level < 3.4%), suggesting limited potential for hypomethylation, unlike temporarily or permanently hypomethylated CpGs which were mostly highly methylated in *Dnmt1*^{CTL} (median level > 85% and 79%, respectively). Some CpG hypermethylation was observed, primarily in a dynamic hypo–hyper pattern (n=94,217) or a latent hypermethylation pattern (n=28,330). The remaining five patterns (temporary hyper, permanent hyper, dynamic hyper–hypo, latent hypo) contained a negligible number of CpGs, totaling ~10K.

Next, we investigated the impact of *Dnmt1* inactivation and rescue in mESCs on histone modification landscapes. We first performed peak calling for H3K4me3, H3K27ac, H3K4me1, H3K27me3 and H3K9me3 in each condition. Compared to *Dnmt1*^{CTL}, the total number of peaks was higher in *Dnmt1*^{INV} for all modifications, while lower peak numbers were observed in *Dnmt1*^{RES}, except for H3K4me3 which remained higher (Figure S1A). Recognizing that peak numbers alone may not fully capture fluctuations in histone modification levels due to variable peak size and enrichment, peak genomic regions across experimental conditions were merged into a common set of regions for each histone modification while also conducting signal enrichment normalization. This enabled statistical and quantitative comparisons between experimental conditions for detecting differentially histone-modified regions (DHMs). DHMs exhibiting either a decrease or an increase in histone modification enrichment, and regions that maintained stable enrichment were computed in *Dnmt1*^{INV} (Figure 2A) and in *Dnmt1*^{RES} (Figure 2B) versus *Dnmt1*^{CTL}. Subsequently, histone-modified regions were classified into histone modification remodulation patterns based on their differential states (decrease, increase or stable) in *Dnmt1*^{INV} and *Dnmt1*^{RES} conditions (Figures 2C and S1B). Although most regions displayed permanent stability of histone modification enrichment (Figure S1B), thousands of DHMs were detected in *Dnmt1*^{INV} and *Dnmt1*^{RES} (Figures 2A-B), with H3K4me3 increase in *Dnmt1*^{INV} being the most striking. Interestingly, DHMs were predominantly condition-specific; the majority of DHMs in *Dnmt1*^{INV} exhibited temporary remodulation (Figure 2D) and in *Dnmt1*^{RES} showed latent remodulation (Figure 2E).

In summary, *Dnmt1* inactivation and rescue induced remodulation of CpG methylation and histone modification landscapes in mESCs, involving permanent, dynamic, and post-rescue responses, offering new insights into the role of DNA methylation maintenance in preserving chromatin integrity. These findings underscored the challenges associated with epigenetic rescue interventions, emphasizing the importance of considering broader epigenomic contexts when perturbing key epigenetic regulators.

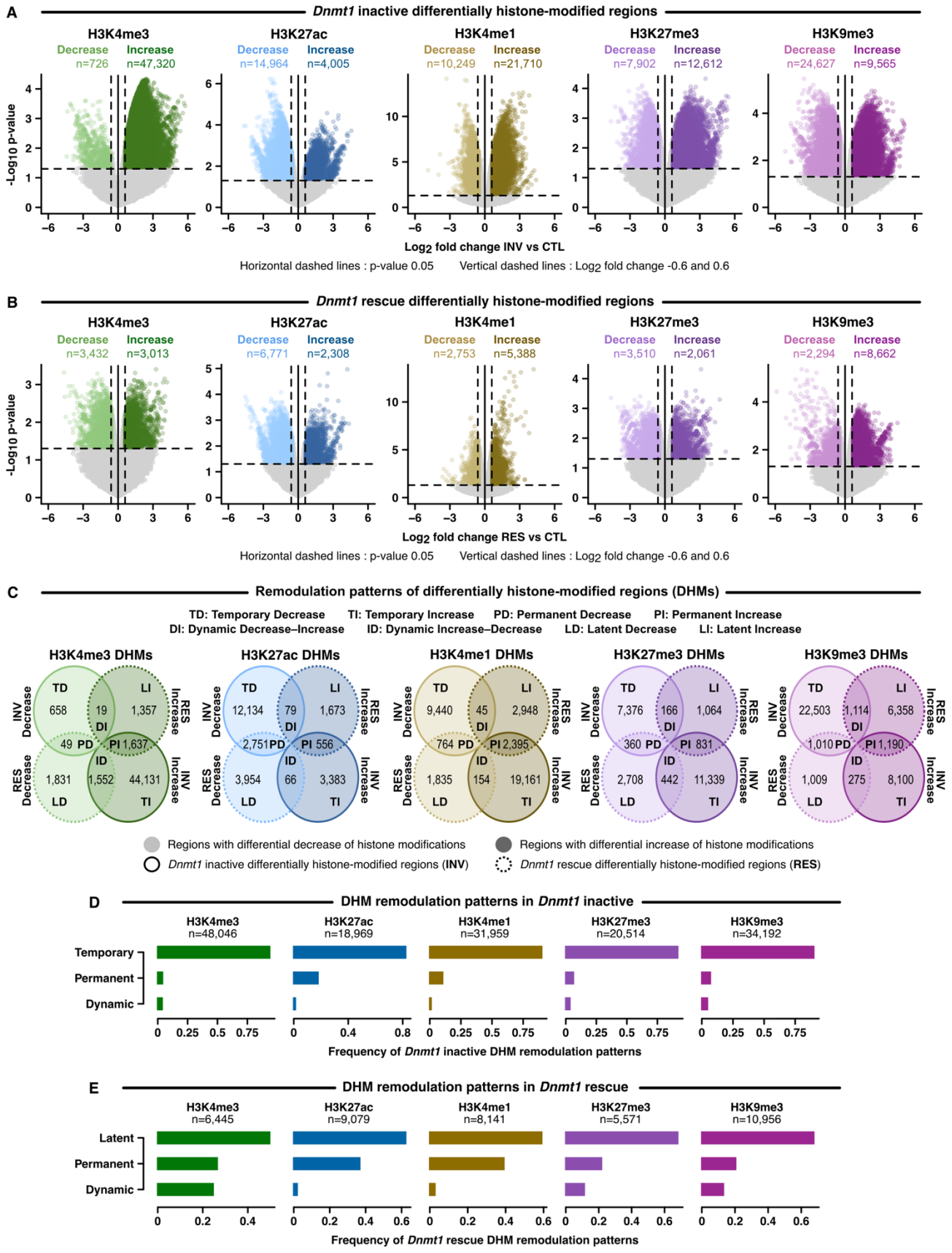
A
Dnmt1 inactive differentially histone-modified regions
H3K4me3
Decrease n=726
Increase n=47,320
H3K27ac
Decrease n=14,964
Increase n=4,005
H3K4me1
Decrease n=10,249
Increase n=21,710
H3K27me3
Decrease n=7,902
Increase n=12,612
H3K9me3
Decrease n=24,627
Increase n=9,565
-Log10 p-value
Log2 fold change INV vs CTL
Horizontal dashed lines : p-value 0.05
Vertical dashed lines : Log2 fold change -0.6 and 0.6
B
Dnmt1 rescue differentially histone-modified regions
H3K4me3
Decrease n=3,432
Increase n=3,013
H3K27ac
Decrease n=6,771
Increase n=2,308
H3K4me1
Decrease n=2,753
Increase n=5,388
H3K27me3
Decrease n=3,510
Increase n=2,061
H3K9me3
Decrease n=2,294
Increase n=8,662
-Log10 p-value
Log2 fold change RES vs CTL
Horizontal dashed lines : p-value 0.05
Vertical dashed lines : Log2 fold change -0.6 and 0.6
C
Remodulation patterns of differentially histone-modified regions (DHMs)
TD: Temporary Decrease
TI: Temporary Increase
PD: Permanent Decrease
PI: Permanent Increase
DI: Dynamic Decrease–Increase
ID: Dynamic Increase–Decrease
LD: Latent Decrease
LI: Latent Increase
H3K4me3 DHMs
TD 658
LI 1,357
DI 19
PD 49
PI 1,637
ID 1,552
LD 1,831
TI 44,131
H3K27ac DHMs
TD 12,134
LI 1,673
DI 79
PD 2,751
PI 556
ID 66
LD 3,954
TI 3,383
H3K4me1 DHMs
TD 9,440
LI 2,948
DI 45
PD 764
PI 2,395
ID 154
LD 1,835
TI 19,161
H3K27me3 DHMs
TD 7,376
LI 1,064
DI 166
PD 360
PI 831
ID 442
LD 2,708
TI 11,339
H3K9me3 DHMs
TD 22,503
LI 6,358
DI 1,114
PD 1,010
PI 1,190
ID 275
LD 1,009
TI 8,100
INV Decrease
RES Increase
RES Decrease
INV Increase
Regions with differential decrease of histone modifications
Regions with differential increase of histone modifications
Dnmt1 inactive differentially histone-modified regions (INV)
Dnmt1 rescue differentially histone-modified regions (RES)
D
DHM remodulation patterns in Dnmt1 inactive
H3K4me3 n=48,046
H3K27ac n=18,969
H3K4me1 n=31,959
H3K27me3 n=20,514
H3K9me3 n=34,192
Temporary
Permanent
Dynamic
Frequency of Dnmt1 inactive DHM remodulation patterns
E
DHM remodulation patterns in Dnmt1 rescue
H3K4me3 n=6,445
H3K27ac n=9,079
H3K4me1 n=8,141
H3K27me3 n=5,571
H3K9me3 n=10,956
Latent
Permanent
Dynamic
Frequency of Dnmt1 rescue DHM remodulation patterns

Figure 2: *Dnmt1* inactivation and rescue in mESCs induces dynamic remodelling of histone modifications, mostly in a condition-specific manner. **(A-B)** Differentially histone-modified regions (DHMs) for H3K4me3, H3K27ac, H3K4me1, H3K27me3 and H3K9me3 in *Dnmt1*^{INV} and *Dnmt1*^{RES} versus *Dnmt1*^{CTL}, respectively, determined by a p-value ≤ 0.05 and $\log_2$ fold change ≤ -0.6 or ≥ 0.6 using the MAnorm2 software. **(C)** Remodulation patterns of DHMs for each histone modification throughout *Dnmt1* inactivation and rescue determined by their differential state in A and B. Temporary: decrease/increase in *Dnmt1*^{INV} & stable in *Dnmt1*^{RES}. Permanent: decrease/increase in both *Dnmt1*^{INV} & *Dnmt1*^{RES}. Dynamic: decrease/increase in *Dnmt1*^{INV} & the opposite in *Dnmt1*^{RES}. Latent: stable in *Dnmt1*^{INV} & decrease/increase in *Dnmt1*^{RES}. **(D-E)** Frequency of DHM remodulation patterns for *Dnmt1*^{INV} and *Dnmt1*^{RES}, respectively, representing the number of DHMs in each pattern divided by the total number of DHMs. *See also Figure S1*.

Permanent CpG hypomethylation is associated with specific genomic location contexts and histone modification remodulation patterns

Acknowledging permanent CpG hypomethylation as a direct outcome of disrupting *Dnmt1* activity, we focussed our attention towards elucidating other factors contributing to this phenomenon, specifically, genomic localization and local histone modification remodulation.

First, we computed the number of CpGs with the potential to undergo permanent hypomethylation, i.e. a sustained methylation decrease of at least 20% throughout *Dnmt1*^{INV} and *Dnmt1*^{RES}. These CpGs had to exhibit a methylation level exceeding 20% in the *Dnmt1*^{CTL} condition and were designated as methylated CpGs (mCpGs). The frequency of mCpGs (ratio of mCpGs to sequenced CpGs) was high (≥ 0.65) across most genomic contexts, except for promoters (0.33) and CGI shores (0.49), which exhibited moderate frequencies, and CpG islands (0.15) and CTCF-bound cCREs (0.24), where frequencies were markedly lower (Figure S2A; Table S1). As for remodulation patterns of DHMs, H3K4me1 and H3K9me3 DHM patterns exhibited high mCpG frequencies overall, while H3K4me3, H3K27ac and H3K27me3 DHM patterns had variable mCpG frequencies (Figure S2B; Table S2). Next, we quantified the number of permanently hypomethylated CpGs and their frequency (ratio of permanently hypomethylated CpGs to mCpGs) (Figures 3A and 3C; Tables S1 and S2). This was followed by the application of Pearson's chi-squared test to discern positive, negative, or neutral association of permanent CpG hypomethylation with genomic location contexts (Figure 3B; Table S1) or with DHM remodulation patterns (Figure 3D, Table S2). Positive associations were observed for ICRs/gDMRs, sex chromosomes, LINEs, LTRs, intergenic, and open sea genomic location contexts. All H3K9me3 DHM patterns, except dynamic increase–decrease, also exhibited positive association along with permanent and latent increase patterns of H3K4me3 and H3K27me3 DHMs. While the permanent increase pattern of H3K27ac DHMs displayed neutral association, it approached significance for positive association. It is noteworthy that, despite having high mCpG frequencies in *Dnmt1*^{CTL}, certain genomic location contexts (e.g. gene bodies, CGI shelves, SINEs) and DHM remodulation patterns (e.g. latent decrease of H3K4me3, temporary increase of H3K4me1, H3K27ac or H3K27me3) were negatively associated with permanent CpG hypomethylation.

In brief, permanent CpG hypomethylation due to inactivation and rescue of *Dnmt1* was positively associated with specific genomic locations beyond ICRs/gDMRs, such as LINEs, LTRs and sex chromosomes, along with specific remodulation patterns of histone modifications, notably H3K9me3, shedding light on the underlying mechanisms of CpG methylation heritability in mESCs.

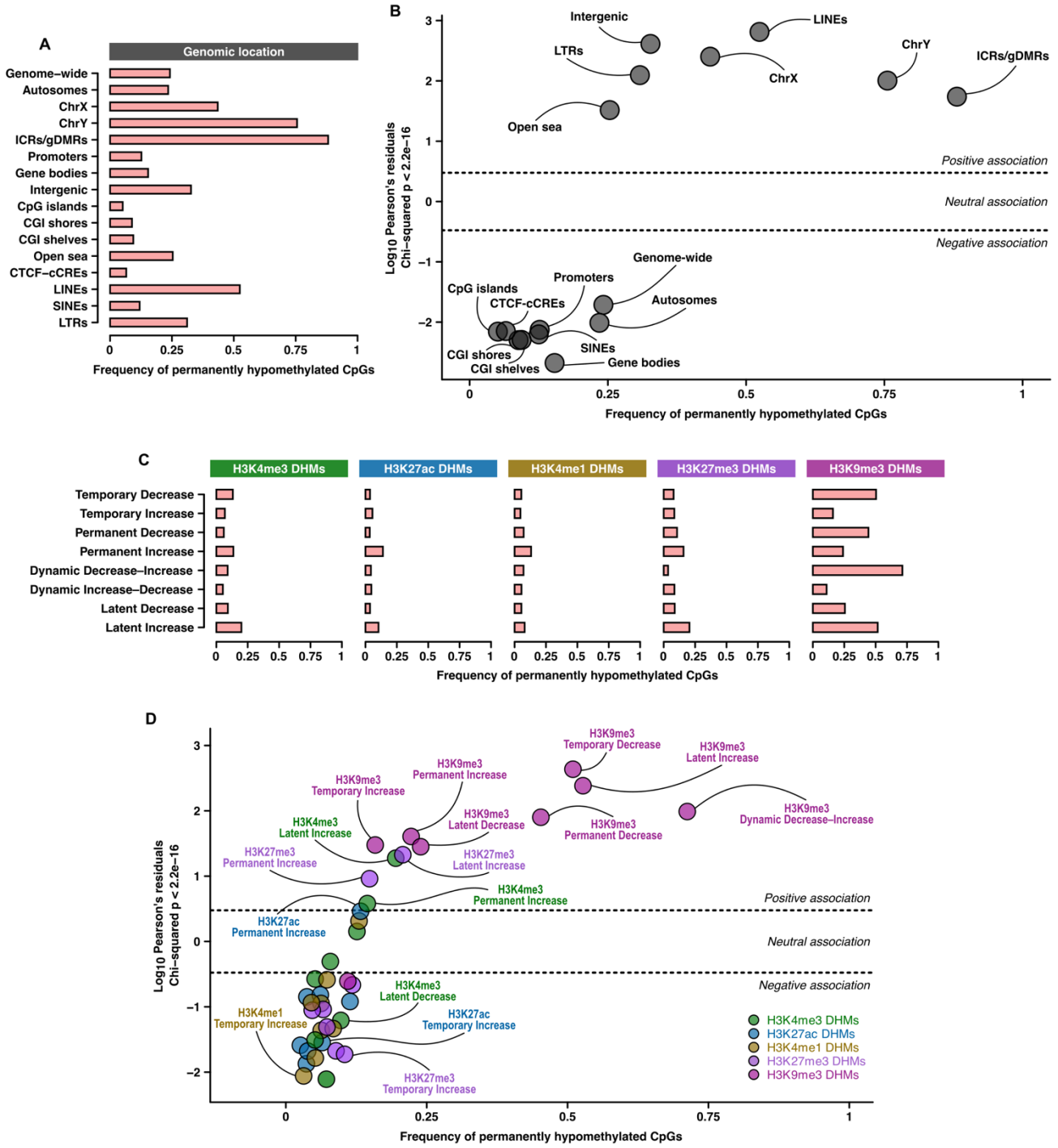

Figure 3: Permanent CpG hypomethylation is associated with specific genomic location contexts and histone modification remodulation patterns. **(A)** Frequency of permanently hypomethylated CpGs per genomic location context. **(B)** Pearson's chi-squared test associating the frequency of permanently hypomethylated CpGs with genomic location contexts. **(C)** Frequency of permanently hypomethylated CpGs in differentially histone-modified regions (DHMs) categorized into remodulation patterns identified in Figure 2C. **(D)** Pearson's chi-squared test associating the frequency of permanently hypomethylated CpGs with DHM remodulation patterns. Frequency of permanently hypomethylated CpGs represents the number of permanently hypomethylated CpGs divided by the number of methylated (methylation level ≥ 20%) CpGs in *Dnmt1*^{CTL}. Pearson's residual ≥ 2 indicates positive, < 2 but > -2 indicates neutral and ≤ -2 indicates negative association. *See also Tables S1 and S2 and Figure S2.*

Epigenetic analysis of ICRs and gDMRs enables the identification of 20 regions with imprinted-like epigenetic and regulatory signatures

ICRs and gDMRs are CpG-rich long-range cis-acting regulatory sites characterized by heritable allele-specific CpG methylation, maintained by the concerted actions of DNMT1, ZFP57, TRIM28 and SETDB1-mediated deposition of broad H3K9me3 domains[28-35]. Leveraging these established features, we aimed to uncover genomic regions exhibiting imprinted-like epigenetic dynamics during inactivation and rescue of *Dnmt1* in mESCs, integrating publicly available datasets to reinforce our methodology.

Among the 26 ICRs and gDMRs[38-61] that were examined, 15 had permanently hypomethylated CpGs, exhibited permanent mean CpG hypomethylation ≥ 10% and overlapped permanently decreased H3K9me3 DHMs (Figure 2C), specifically within broad H3K9me3 domains (≥ 3000 bp) (Figure 4A; Table S3). The remaining 11 did not meet those criteria in addition to having low mCpG frequencies (≤ 0.25) and low mean CpG methylation levels in *Dnmt1*^{CTL} (median < 4%), thus were excluded from further analysis. To identify regions with imprinted-like signatures that we termed gDMR-like regions, we employed publicly available mESC allele-specific methylated regions identified by the Smith Lab[62] in data from Leung et al.[34] We filtered allele-specific methylated regions based on their non-overlap with ICRs/gDMRs and on them exhibiting epigenetic dynamics akin to those observed in the 15 selected ICRs/gDMRs: presence of permanently hypomethylated CpGs, permanent mean CpG hypomethylation ≥ 10% and overlapping permanently decreased H3K9me3 DHMs within broad domains ≥ 3000 bp. Ultimately, 20 gDMR-like regions were retained, named according to their intersection with or proximity to genes (Figure 4B; Table S3).

In comparison to the selected 15 ICRs/gDMRs, gDMR-like regions also had high frequencies of mCpGs in *Dnmt1*^{CTL} and high frequencies of permanently hypomethylated CpGs (Figure S3A), along with comparable mean CpG methylation levels in *Dnmt1*^{CTL} (Figure S3B). However, gDMR-like regions displayed lower CpG density (Figure S3C) and less severe permanent mean CpG hypomethylation (Figure S3D) than the selected 15 ICRs/gDMRs. Next, we computed mean histone modification RPKM levels within each region in *Dnmt1*^{CTL}, *Dnmt1*^{INV} and *Dnmt1*^{RES} (Table S3), employing z-score normalization to reveal epigenetic remodulation dynamics other than permanent CpG hypomethylation and H3K9me3 decrease (Figure 4C). Notably prevalent among ICRs, gDMRs and gDMR-like regions were a temporary sharp elevation in H3K4me3 levels and permanently higher levels of H3K4me1, with variable fluctuations in H3K27ac and H3K27me3 levels.

We then measured mean CpG methylation levels of each region in mouse oocytes and sperm using data from Wang et al.[63] analyzed by the Smith Lab[62] to explore germline inheritance of allele-specific CpG methylation in gDMR-like regions (Table S3). ICRs/gDMRs exhibited anticipated oocyte- or sperm-specific CpG methylation, except for the *Meg3* ICR (Figure 4D). Differential CpG methylation between gametes was also observed in gDMR-like regions (Figure 4E); for instance, *Repin1* and *Errfi1 downstream* showed oocyte specificity. Displaying gamete and mESC epigenetic profiles of *Repin1* and *Errfi1 downstream* gDMR-like regions alongside those of oocyte-specific ICRs *Mest* and *Plagl1* clearly showcased CpG hypermethylation in oocytes versus sperm and similar remodulation dynamics during *Dnmt1* inactivation and rescue in mESCs, especially for CpG methylation, H3K4me3, H3K4me1, and H3K9me3 (Figure S3E). While the distinction of gamete-specific CpG methylation in gDMR-like regions was generally less pronounced compared to ICRs/gDMRs, they all exhibited substantial levels (> 35%) in at least one gamete (Figure 4D-E; Table S3), suggesting germline inheritance of CpG methylation profiles. CpG methylation may be present in both gametes initially and retained on only one allele post-fertilization due to other gamete-specific epigenetic marks or regulatory factors.

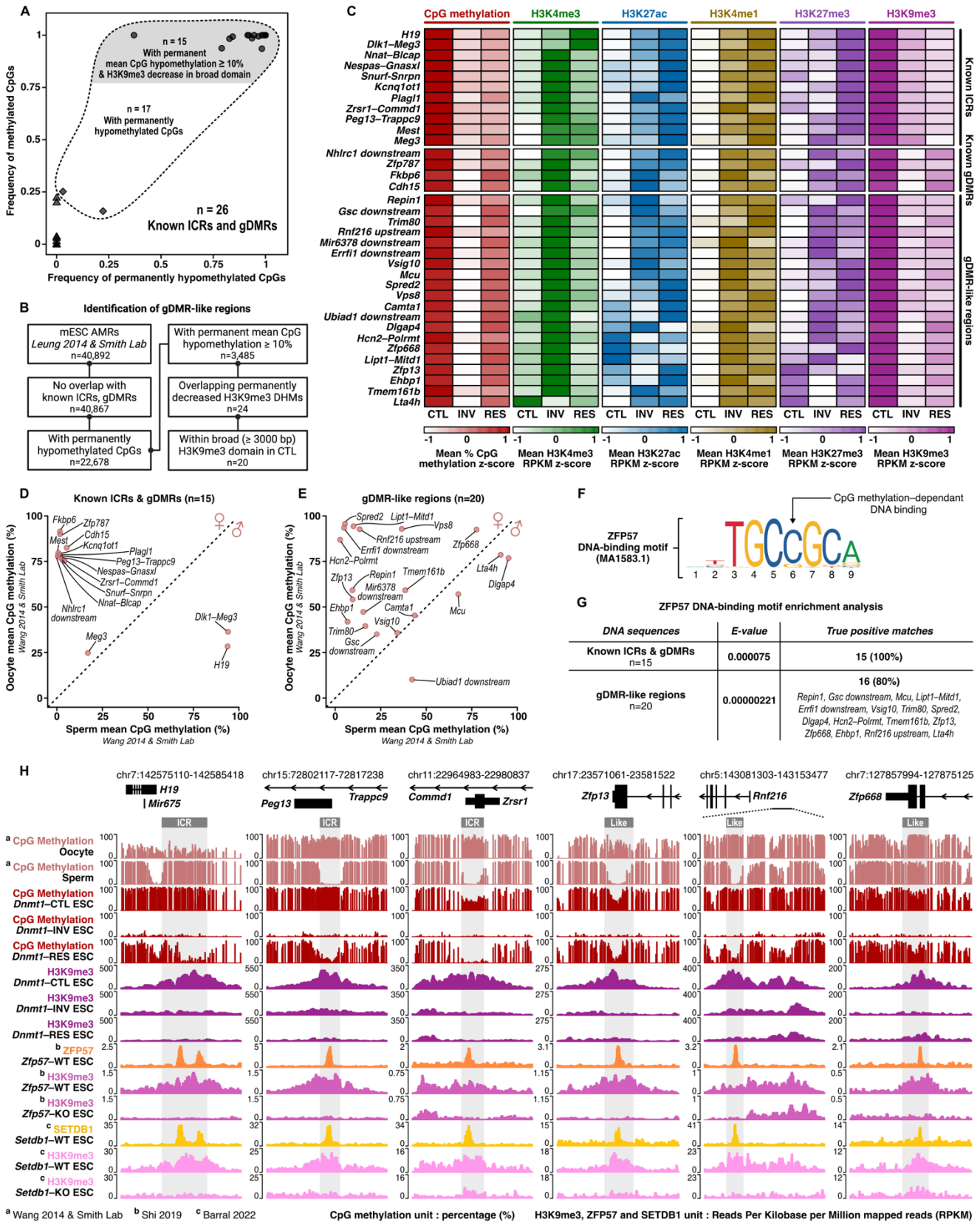
A
n = 15
With permanent
mean CpG hypomethylation ≥ 10%
& H3K9me3 decrease in broad domain
n = 17
With permanently
hypomethylated CpGs
n = 26
Known ICRs and gDMRs
Frequency of methylated CpGs
Frequency of permanently hypomethylated CpGs
B
Identification of gDMR-like regions
mESC AMRs
Leung 2014 & Smith Lab
n=40,892
No overlap with
known ICRs, gDMRs
n=40,867
With permanently
hypomethylated CpGs
n=22,678
With permanent mean CpG
hypomethylation ≥ 10%
n=3,485
Overlapping permanently
decreased H3K9me3 DHMs
n=24
Within broad (≥ 3000 bp)
H3K9me3 domain in CTL
n=20
C
CpG methylation
H3K4me3
H3K27ac
H3K4me1
H3K27me3
H3K9me3
Known ICRs
Known gDMRs
gDMR-like regions
CTL INV RES
Mean % CpG methylation z-score
Mean H3K4me3 RPKM z-score
Mean H3K27ac RPKM z-score
Mean H3K4me1 RPKM z-score
Mean H3K27me3 RPKM z-score
Mean H3K9me3 RPKM z-score
D
Known ICRs & gDMRs (n=15)
Oocyte mean CpG methylation (%)
Sperm mean CpG methylation (%)
Wang 2014 & Smith Lab
E
gDMR-like regions (n=20)
F
CpG methylation–dependant DNA binding
ZFP57 DNA-binding motif (MA1583.1)
G
ZFP57 DNA-binding motif enrichment analysis
DNA sequences | E-value | True positive matches
Known ICRs & gDMRs n=15 | 0.000075 | 15 (100%)
gDMR-like regions n=20 | 0.00000221 | 16 (80%) Repin1, Gsc downstream, Mcu, Lipt1–Mitd1, Errfi1 downstream, Vsig10, Trim80, Spred2, Dlgap4, Hcn2–Polrmt, Tmem161b, Zfp13, Zfp668, Ehbp1, Rnf216 upstream, Lta4h
H
chr7:142575110-142585418
chr15:72802117-72817238
chr11:22964983-22980837
chr17:23571061-23581522
chr5:143081303-143153477
chr7:127857994-127875125
ICR
Like
CpG Methylation Oocyte
CpG Methylation Sperm
CpG Methylation Dnmt1–CTL ESC
CpG Methylation Dnmt1–INV ESC
CpG Methylation Dnmt1–RES ESC
H3K9me3 Dnmt1–CTL ESC
H3K9me3 Dnmt1–INV ESC
H3K9me3 Dnmt1–RES ESC
ZFP57 Zfp57–WT ESC
H3K9me3 Zfp57–WT ESC
H3K9me3 Zfp57–KO ESC
SETDB1 Setdb1–WT ESC
H3K9me3 Setdb1–WT ESC
H3K9me3 Setdb1–KO ESC
a Wang 2014 & Smith Lab
b Shi 2019
c Barral 2022
CpG methylation unit : percentage (%)
H3K9me3, ZFP57 and SETDB1 unit : Reads Per Kilobase per Million mapped reads (RPKM)

Figure 4: Epigenetic analysis of ICRs and gDMRs enables the identification of 20 regions with imprinted-like epigenetic and regulatory signatures. **(A)** Selection of 15 ICRs and gDMRs based on four criteria: permanently hypomethylated CpGs ≥ 1, permanent mean CpG hypomethylation ≥ 10%, overlapping permanently decreased H3K9me3 DHMs and located within H3K9me3 broad domains (≥ 3000 bp) in *Dnmt1*^{CTL}. **(B)** Workflow for identifying gDMR-like regions among mESC allele-specific methylated regions based on the four criteria in A. **(C)** Z-score normalization of epigenetic modification levels in *Dnmt1*^{CTL}, *Dnmt1*^{INV} and *Dnmt1*^{RES} for selected ICRs/gDMRs and gDMR-like regions. **(D-E)** Mean CpG methylation levels in oocytes versus sperm for selected ICRs/gDMRs and gDMR-like regions, respectively. **(F)** ZFP57 DNA binding motif MA1583.1. **(G)** Enrichment of ZFP57 DNA binding motif MA1583.1 in selected ICRs/gDMRs and gDMR-like regions. (H) Genomic signal tracks for *H19*, *Peg13–Trappc9* and *Zrsr1–Commd1* ICRs and *Zfp13*, *Rnf216 upstream* and *Zfp668* gDMR-like regions showing CpG methylation in gametes and *Dnmt1*$^{tet/tet}$ mESCs, H3K9me3 in *Dnmt1*$^{tet/tet}$ mESCs, *Zfp57* WT and KO mESCs and *Setdb1* WT and KO mESCs, ZFP57 binding in *Zfp57* WT mESCs and SETDB1 binding in *Setdb1* WT mESCs. *See also Table S3 and Figures S3 and S4.*

To further investigate regulation of gDMR-like regions by genomic imprinting mechanisms, we conducted enrichment analysis of ZFP57 DNA-binding motif (Figure 4F), revealing positive matches with 80% of gDMR-like regions and, predictably, with 100% of ICRs/gDMRs (Figure 4G). Moreover, the permanent decrease of broad H3K9me3 detected in our model was strikingly mirrored in *Zfp57* KO mESCs[35] and *Setdb1* KO mESCs[64] for ICRs (e.g. *H19*, *Peg13–Trappc9*, *Zrsr1–Commd1*) and gDMR-like regions (e.g. *Zfp13*, *Rnf216 upstream*, *Zf668*), with binding of ZFP57 and SETDB1 coinciding within these regions (Figure 4H). This was observed regardless of gamete-specific CpG methylation, as evidenced by the *Zfp668* gDMR-like region displaying nearly identical CpG methylation profiles in both gametes.

Finally, we examined significant gene expression dysregulation (adjusted p-value ≤ 0.05) in *Dnmt1*^{INV} and *Dnmt1*^{RES} versus *Dnmt1*^{CTL} for imprinted genes controlled by the selected 15 ICRs/gDMRs (Figures S4A-B, Table S4) and for genes associated with gDMR-like regions (Figures S4C-D, Table S4). As expected, numerous imprinted genes showed significant permanent downregulation (e.g. *Igf2*, *Trappc9*, *Cdkn1c*, *Phlda2*) or upregulation (e.g. *Mest*, *Plagl1*, *H19*, *Zrsr1*), mostly exhibiting strong dysregulation ($\log_2$ fold change ≤ -0.6 or ≥ 0.6). Some genes associated with gDMR-like regions were also significantly permanently downregulated (*Zfp668*) or upregulated (*Repin1*, *Rnf216*, *Hcn2*, *Vsig10*), albeit with milder dysregulation. Nevertheless, 17 out of the 22 genes associated with gDMR-like regions were dysregulated in *Dnmt1*^{INV}, suggesting a transcriptional impact linked to de-repression of their gDMR-like region. However, considering that gDMR-like regions are not within gene promoters (Table S3) and given their fluctuations in enhancer-related H3K4me1 and H3K27ac, assessing their direct influence on gene expression would require a targeted de-repression approach such as CRISPR-mediated demethylation.

To summarize, we uncovered 20 gDMR-like regions with epigenetic and regulatory features closely resembling those of ICRs/gDMRs. While all gDMR-like regions exhibited CpG methylation in gametes, many lacked gamete specificity, possibly hinting at nuanced mechanisms in germline inheritance of allele-specific CpG methylation.

Permanent de-repression of MERVL and MT2 LTRs may be linked to gene transcript chimerism

De-repression of transposable elements can influence gene expression, genomic stability, and cellular functions, with DNA methylation being crucial for their silencing[65]. The significant susceptibility of LTRs and LINEs to permanent CpG hypomethylation during *Dnmt1* inactivation and rescue in mESCs (Figure 3B) led us to investigate the resulting effects on their transcription.

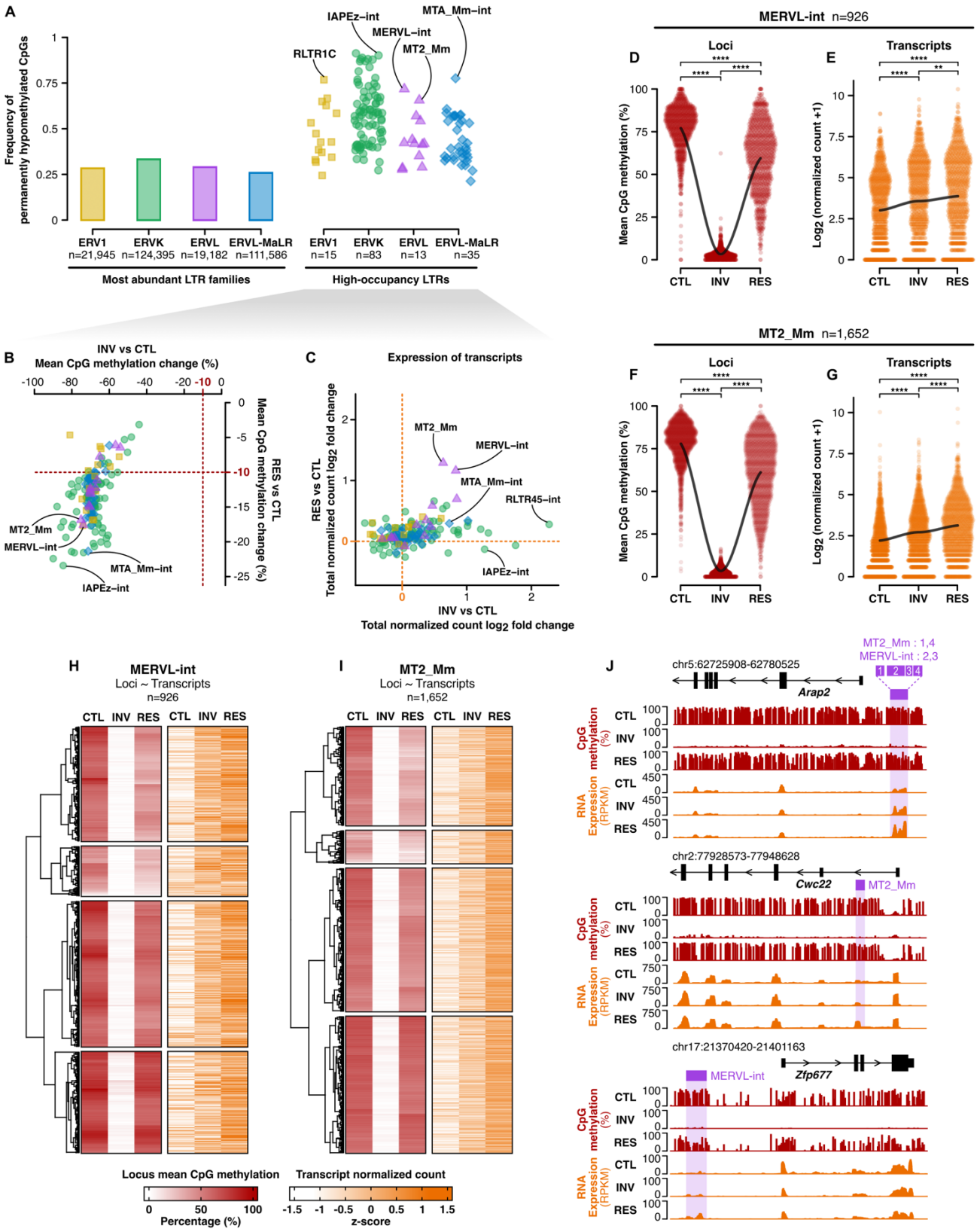
A
Frequency of permanently hypomethylated CpGs
ERV1 n=21,945
ERVK n=124,395
ERVL n=19,182
ERVL-MaLR n=111,586
Most abundant LTR families
IAPEz–int
MTA_Mm–int
MERVL–int
MT2_Mm
RLTR1C
ERV1 n=15
ERVK n=83
ERVL n=13
ERVL-MaLR n=35
High-occupancy LTRs
MERVL-int n=926
D
Loci
E
Transcripts
Mean CpG methylation (%)
Log2 (normalized count +1)
CTL
INV
RES
B
INV vs CTL
Mean CpG methylation change (%)
RES vs CTL
Mean CpG methylation change (%)
C
Expression of transcripts
RES vs CTL
Total normalized count log2 fold change
INV vs CTL
Total normalized count log2 fold change
RLTR45–int
MT2_Mm n=1,652
F
G
H
MERVL-int
Loci ~ Transcripts
n=926
I
MT2_Mm
Loci ~ Transcripts
n=1,652
Locus mean CpG methylation
Percentage (%)
Transcript normalized count
z-score
J
chr5:62725908-62780525
Arap2
MT2_Mm : 1,4
MERVL-int : 2,3
chr2:77928573-77948628
Cwc22
MT2_Mm
chr17:21370420-21401163
Zfp677
MERVL-int
CpG methylation (%)
RNA Expression (RPKM)

Figure 5: Permanent de-repression of MERVL and MT2 LTRs may be linked to gene transcript chimerism. **(A)** Frequency of permanently hypomethylated CpGs in the most abundant LTR families and in high-occupancy LTRs (genomic occurrences ≥ 500). **(B-C)** Change in mean CpG methylation levels and $\log_2$ fold change of total RNA-seq normalized counts, respectively, of high-occupancy LTRs in *Dnmt1*^{INV} and *Dnmt1*^{RES} versus *Dnmt1*^{CTL}. **(D-E)** Pairwise comparisons of MERVL-int locus-specific mean CpG methylation levels and RNA-seq normalized counts, respectively, in *Dnmt1*^{CTL}, *Dnmt1*^{INV} and *Dnmt1*^{RES} using the Wilcoxon rank sum test with Benjamini-Hochberg p-value adjustment. **(F-G)** Pairwise comparisons of MT2-Mm locus-specific mean CpG methylation levels and RNA-seq normalized counts, respectively, in *Dnmt1*^{CTL}, *Dnmt1*^{INV} and *Dnmt1*^{RES} using the Wilcoxon rank sum test with Benjamini-Hochberg p-value adjustment. **(H-I)** Z-score normalization of mean CpG methylation level and RNA-seq normalized count for each MERVL-int and MT2_Mm locus. **(J)** Genomic signal tracks showing CpG methylation and RNA expression for MERVL-int and MT2-Mm loci proximal to gene transcription start sites in *Dnmt1*^{CTL}, *Dnmt1*^{INV} and *Dnmt1*^{RES}. *See also Table S5*.

We initially investigated whether specific LTR and LINE families showed distinct propensities for permanent CpG hypomethylation. The frequency of permanently hypomethylated CpGs within the most abundant LTR families (Figure 5A)—ERV1 (0.28), ERVK (0.33), ERVL (0.29), and ERVL-MaLR (0.26)—did not substantially deviate from the overall frequency in LTRs (0.31) (Figure 3A). The frequency in L1 LINEs (0.52) (Figure S5A), the most abundant LINE family, was identical to all LINEs combined (Figure 3A). Though, when computing the frequencies of permanently hypomethylated CpGs specifically in high-occupancy elements (i.e. genomic occurrences ≥ 500), the vast majority had strikingly higher frequencies (Figures 5A and S5A). We thus focused on high-occupancy elements to explore if their permanent CpG hypomethylation affected their transcription. Mean CpG methylation levels and total normalized RNA-seq counts of all loci combined were measured for each high-occupancy element across conditions. All high-occupancy L1 elements exhibited permanent mean CpG hypomethylation ≥ 10% (Figure S5B), but none showed major alterations in transcription (total normalized count $\log_2$ fold change > -1 and < 1 in *Dnmt1*^{INV} and *Dnmt1*^{RES} versus *Dnmt1*^{CTL}) (Figure S5C). Turning towards high-occupancy LTR elements, MERVL-int and MT2_Mm emerged as the sole elements demonstrating two key characteristics: permanent mean CpG hypomethylation ≥ 10% (Figure 5B) and notable gradual increase in transcription throughout *Dnmt1* inactivation and rescue, culminating with a $\log_2$ fold change ≥ 1 in *Dnmt1*^{RES} versus *Dnmt1*^{CTL} (Figure 5C). Given the evidence supporting the pivotal roles of MERVL-int and MT2_Mm in zygotic genome activation[66-68] and potency state transitions[69,70], we undertook a deeper analysis of locus-specific CpG methylation and transcription dynamics. Overall, MERVL-int and MT2_Mm showed highly significant decrease in locus-specific mean CpG methylation levels and increase in locus-specific transcript levels in *Dnmt1*^{INV} and *Dnmt1*^{RES} compared to *Dnmt1*^{CTL} (Figures 5D-G; Table S5). Upon examination of each locus, permanent and gradual increase in transcription occurred at loci exhibiting either temporary or permanent CpG hypomethylation (Figures 5H-I). Furthermore, MERVL-int and MT2_Mm upregulation proximal to gene transcription start sites (TSS) (e.g. *Arap2*, *Cwc22*, *Zfp677*) implies the generation of associated chimeric gene transcripts (Figure 5J).

To sum up, high-occupancy LTR and LINE elements exhibited a heightened susceptibility to permanent CpG hypomethylation during *Dnmt1* inactivation and rescue in mESCs. MERVL-int and MT2_Mm LTRs stood out for displaying increased transcription even in instances where CpG hypomethylation was only temporary, potentially generating associated gene transcript chimerism.

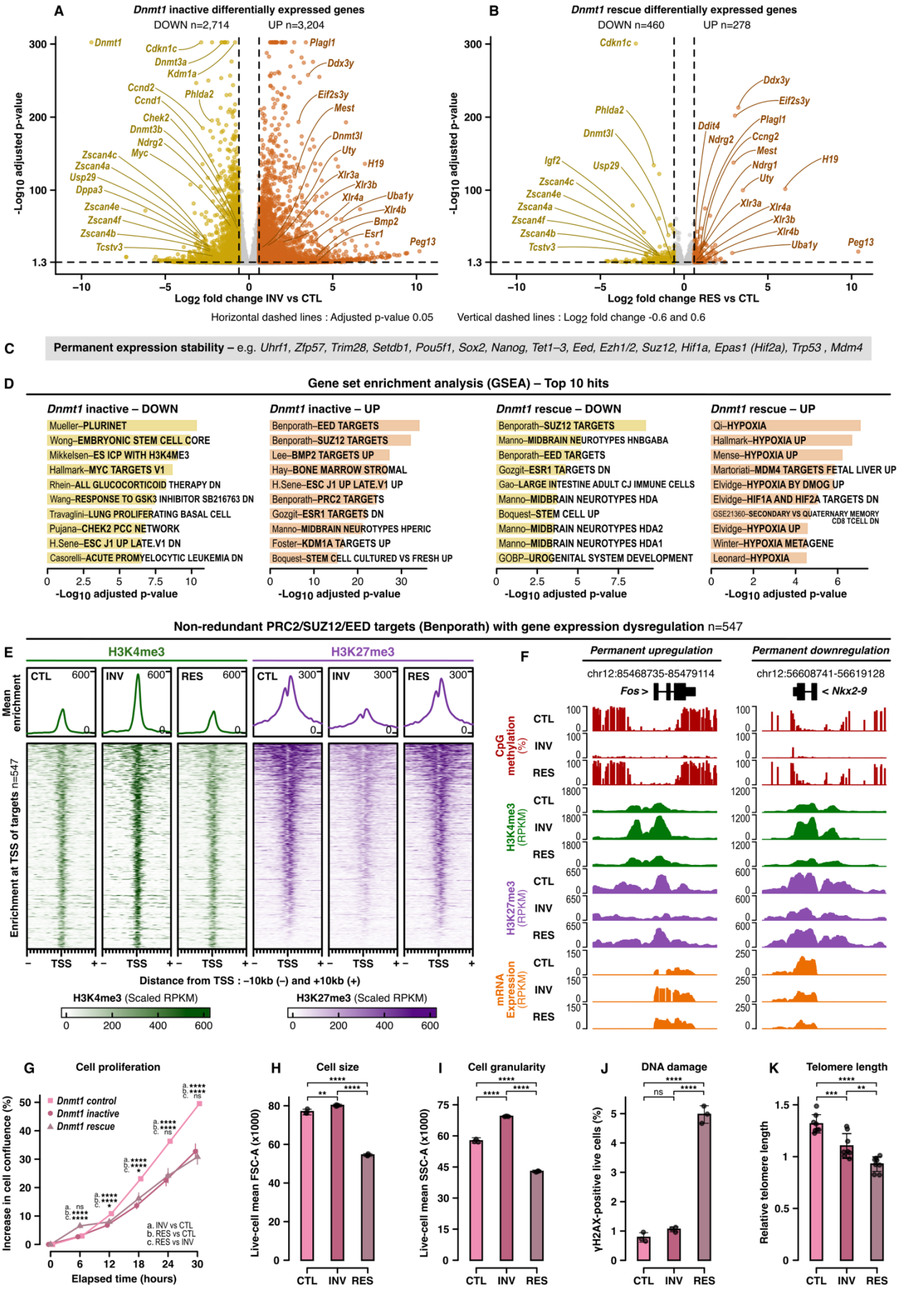
A
Dnmt1 inactive differentially expressed genes
DOWN n=2,714
UP n=3,204
-Log10 adjusted p-value
Log2 fold change INV vs CTL
Horizontal dashed lines : Adjusted p-value 0.05
B
Dnmt1 rescue differentially expressed genes
DOWN n=460
UP n=278
Log2 fold change RES vs CTL
Vertical dashed lines : Log2 fold change -0.6 and 0.6
C
Permanent expression stability – e.g. Uhrf1, Zfp57, Trim28, Setdb1, Pou5f1, Sox2, Nanog, Tet1–3, Eed, Ezh1/2, Suz12, Hif1a, Epas1 (Hif2a), Trp53 , Mdm4
D
Gene set enrichment analysis (GSEA) – Top 10 hits
Dnmt1 inactive – DOWN
Mueller–PLURINET
Wong–EMBRYONIC STEM CELL CORE
Mikkelsen–ES ICP WITH H3K4ME3
Hallmark–MYC TARGETS V1
Rhein–ALL GLUCOCORTICOID THERAPY DN
Wang–RESPONSE TO GSK3 INHIBITOR SB216763 DN
Travaglini–LUNG PROLIFERATING BASAL CELL
Pujana–CHEK2 PCC NETWORK
H.Sene–ESC J1 UP LATE.V1 DN
Casorelli–ACUTE PROMYELOCYTIC LEUKEMIA DN
Dnmt1 inactive – UP
Benporath–EED TARGETS
Benporath–SUZ12 TARGETS
Lee–BMP2 TARGETS UP
Hay–BONE MARROW STROMAL
H.Sene–ESC J1 UP LATE.V1 UP
Benporath–PRC2 TARGETS
Gozgit–ESR1 TARGETS DN
Manno–MIDBRAIN NEUROTYPES HPERIC
Foster–KDM1A TARGETS UP
Boquest–STEM CELL CULTURED VS FRESH UP
Dnmt1 rescue – DOWN
Benporath–SUZ12 TARGETS
Manno–MIDBRAIN NEUROTYPES HNBGABA
Benporath–EED TARGETS
Gozgit–ESR1 TARGETS DN
Gao–LARGE INTESTINE ADULT CJ IMMUNE CELLS
Manno–MIDBRAIN NEUROTYPES HDA
Boquest–STEM CELL UP
Manno–MIDBRAIN NEUROTYPES HDA2
Manno–MIDBRAIN NEUROTYPES HDA1
GOBP–UROGENITAL SYSTEM DEVELOPMENT
Dnmt1 rescue – UP
Qi–HYPOXIA
Hallmark–HYPOXIA UP
Mense–HYPOXIA UP
Martoriati–MDM4 TARGETS FETAL LIVER UP
Elvidge–HYPOXIA BY DMOG UP
Elvidge–HIF1A AND HIF2A TARGETS DN
GSE21360–SECONDARY VS QUATERNARY MEMORY CD8 TCELL DN
Elvidge–HYPOXIA UP
Winter–HYPOXIA METAGENE
Leonard–HYPOXIA
-Log10 adjusted p-value
Non-redundant PRC2/SUZ12/EED targets (Benporath) with gene expression dysregulation n=547
E
H3K4me3
H3K27me3
CTL
INV
RES
Mean enrichment
Enrichment at TSS of targets n=547
TSS
Distance from TSS : –10kb (–) and +10kb (+)
H3K4me3 (Scaled RPKM)
H3K27me3 (Scaled RPKM)
F
Permanent upregulation
Permanent downregulation
chr12:85468735-85479114
chr12:56608741-56619128
Fos >
< Nkx2-9
CpG methylation (%)
H3K4me3 (RPKM)
H3K27me3 (RPKM)
mRNA Expression (RPKM)
G
Cell proliferation
Dnmt1 control
Dnmt1 inactive
Dnmt1 rescue
Increase in cell confluence (%)
Elapsed time (hours)
a. INV vs CTL
b. RES vs CTL
c. RES vs INV
H
Cell size
Live-cell mean FSC-A (x1000)
I
Cell granularity
Live-cell mean SSC-A (x1000)
J
DNA damage
γH2AX-positive live cells (%)
K
Telomere length
Relative telomere length

Figure 6: Gene expression dysregulation, genomic instability, and dysfunction of cellular processes. **(A-B)** Differentially expressed genes in *Dnmt1*^{INV} and *Dnmt1*^{RES} versus *Dnmt1*^{CTL}, respectively, determined by an adjusted p-value ≤ 0.05 and $\log_2$ fold change ≤ -0.6 or ≥ 0.6 using mRNA sequencing analyzed with the DESeq2 software. **(C)** Notable genes with stable expression in *Dnmt1*^{INV} and *Dnmt1*^{RES} versus *Dnmt1*^{CTL}. **(D)** Gene set enrichment analysis for down- and upregulated genes in *Dnmt1*^{INV} and *Dnmt1*^{RES}. **(E)** Signal enrichment of H3K4me3 and H3K27me3 in *Dnmt1*^{CTL}, *Dnmt1*^{INV} and *Dnmt1*^{RES} at transcription start sites of PRC2/SUZ12/EED non-redundant targets exhibiting gene expression dysregulation in *Dnmt1*^{INV} and/or *Dnmt1*^{RES} identified in D. RPKM values were scaled between 0 and 0.99 quantiles to mitigate the presence of outliers. **(F)** Genomic signal tracks showing CpG methylation, H3K4me3, H3K27me3 and mRNA expression for PRC2/SUZ12/EED targets *Fos* and *Nkx2-9* in *Dnmt1*^{CTL}, *Dnmt1*^{INV} and *Dnmt1*^{RES}. **(G)** Pairwise comparisons of cell proliferation rate for *Dnmt1*^{CTL}, *Dnmt1*^{INV} and *Dnmt1*^{RES} measured by the increase in confluency over 30 hours. **(H-J)** Pairwise comparisons of live-cell mean forward scatter area (FSC-A; cell size), live-cell mean side scatter area (SSC-A; cell granularity) and percentage of γH2AX-positive live cells (DNA damage), respectively, in *Dnmt1*^{CTL}, *Dnmt1*^{INV} and *Dnmt1*^{RES} measured by FACS. **(K)** Pairwise comparisons of relative telomere length in *Dnmt1*^{CTL}, *Dnmt1*^{INV} and *Dnmt1*^{RES} measured by qPCR and the delta-delta Ct method, with normalization to reference single-copy gene *Rplp0* and relativization to reference DNA from R1 mESCs. All pairwise comparisons were conducted using one-way ANOVA with Tukey's HSD test with p-value adjustment. *See also Tables S6 and S7 and Figures S6 and S7*.

Gene expression dysregulation, genomic instability, and dysfunction of cellular processes

Dnmt1 inactivation and rescue in mESCs prompted extensive epigenomic remodeling. To ascertain whether these alterations reflected epigenomic instability, gene expression analysis beyond imprinted genes and examination of genomic stability and cellular processes were imperative.

We first examined significantly differentially expressed genes (adjusted p-value ≤ 0.05) in *Dnmt1*^{INV} and *Dnmt1*^{RES} conditions versus *Dnmt1*^{CTL}, focusing on genes exhibiting dysregulation of considerable magnitude ($\log_2$ fold change ≤ -0.6 or ≥ 0.6). Thousands of genes were dysregulated in *Dnmt1*^{INV} (downregulated: n=2,714; upregulated; n=3,204) (Figure 6A; Table S6), whereas in *Dnmt1*^{RES}, the number was notably reduced but still in the hundreds (downregulated: n=460; upregulated; n=278) (Figure 6B; Table S6). To reveal patterns of gene expression dysregulation, we categorized genes based on their downregulation, upregulation, or stable expression in *Dnmt1*^{INV} and *Dnmt1*^{RES} (Figures 6C and S6A). Interestingly, *Dnmt3a* and *Dnmt3b* exhibited temporary downregulation, whereas *Dnmt3l* demonstrated dynamic up- and downregulation. Conversely, other key players in DNA methylation such as *Uhrf1*, *Tet1-3*, *Zfp57*, and *Trim28*, maintained stable expression. *Kdm1a*, known for gene repression via H3K4 demethylation, was notably temporarily downregulated, possibly contributing to the marked H3K4me3 increase in *Dnmt1*^{INV} (Figure 2A). Dysregulation extended to cell cycle regulators, with *Myc*, *Ccnd1-2*, and *Chek2* exhibiting temporary downregulation, and *Ccng2* showing latent upregulation. Additionally, cellular stress and DNA damage response genes were affected, with *Ndrg1* and *Ddit4* showing latent upregulation, and *Ndrg1* showing dynamic down- and upregulation. Potency state regulators were also dysregulated, including temporary downregulation of *Dppa3* and permanent downregulation of *Zscan4a-f* and *Tcstv3*, the latter two being specifically recognized for their role in telomere elongation[71,72]. Notably, an increase and spreading of repressive H3K9me3 across the promoters and gene bodies of *Zscan4a* and *Zscan4d* was evident in *Dnmt1*^{INV} and *Dnmt1*^{RES} (Figure S6B). Moreover, permanent upregulation of *Xlr3a-b* and *Xlr4a-b*, part of an X-linked cluster known for tissue-specific imprinted gene expression in mice[73], and of *Uba1y*, *Eif2s3y*, *Uty*, and *Ddx3y* within a Y-linked cluster were of particular interest given the significant susceptibility of sex chromosomes to permanent CpG hypomethylation (Figure 3B). In fact, promoters of *Xlr3a*, *Xlr4a*, *Eif2s3y* and *Uty* showed permanent CpG hypomethylation and increase of permissive H3K4me3 and H3K27ac in *Dnmt1*^{INV} and *Dnmt1*^{RES} (Figure S6C).

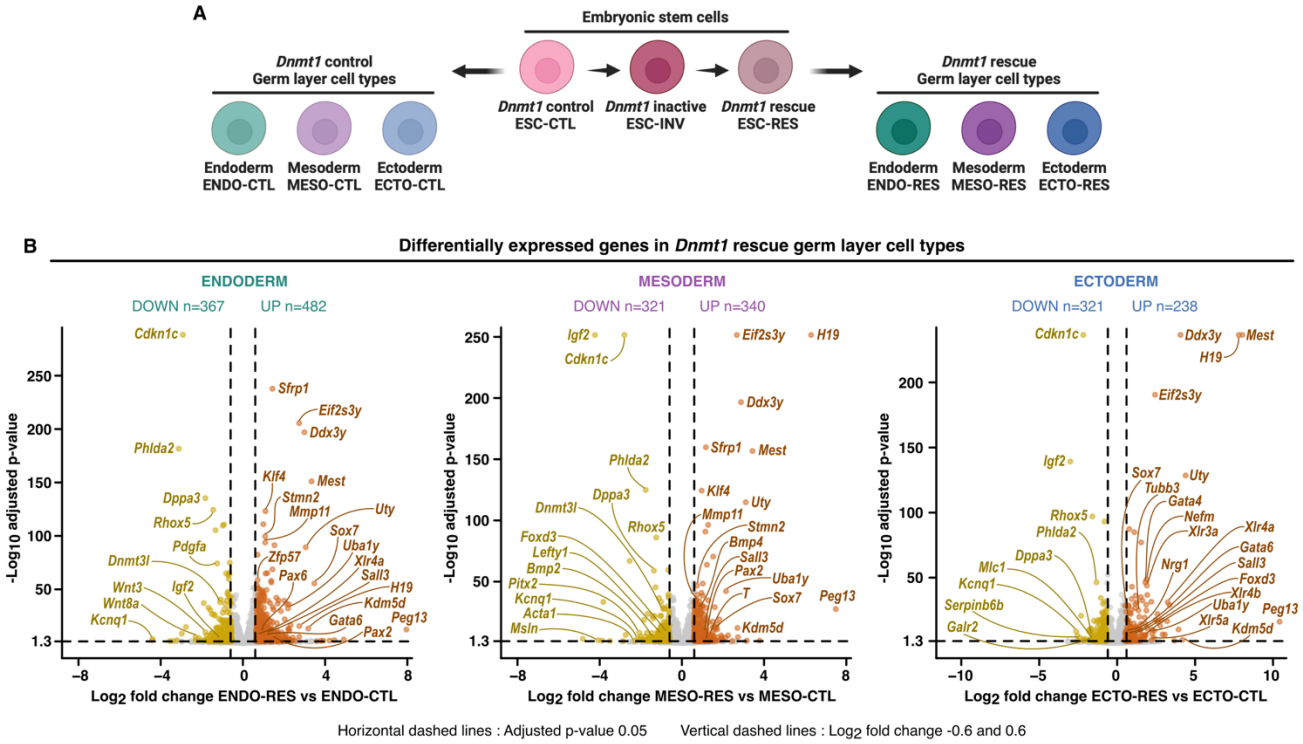
A
Embryonic stem cells
Dnmt1 control Germ layer cell types
Dnmt1 control ESC-CTL
Dnmt1 inactive ESC-INV
Dnmt1 rescue ESC-RES
Dnmt1 rescue Germ layer cell types
Endoderm ENDO-CTL
Mesoderm MESO-CTL
Ectoderm ECTO-CTL
Endoderm ENDO-RES
Mesoderm MESO-RES
Ectoderm ECTO-RES
B
Differentially expressed genes in Dnmt1 rescue germ layer cell types
ENDODERM
DOWN n=367
UP n=482
MESODERM
DOWN n=321
UP n=340
ECTODERM
DOWN n=321
UP n=238
-Log10 adjusted p-value
Log2 fold change ENDO-RES vs ENDO-CTL
Log2 fold change MESO-RES vs MESO-CTL
Log2 fold change ECTO-RES vs ECTO-CTL
Horizontal dashed lines : Adjusted p-value 0.05
Vertical dashed lines : Log2 fold change -0.6 and 0.6

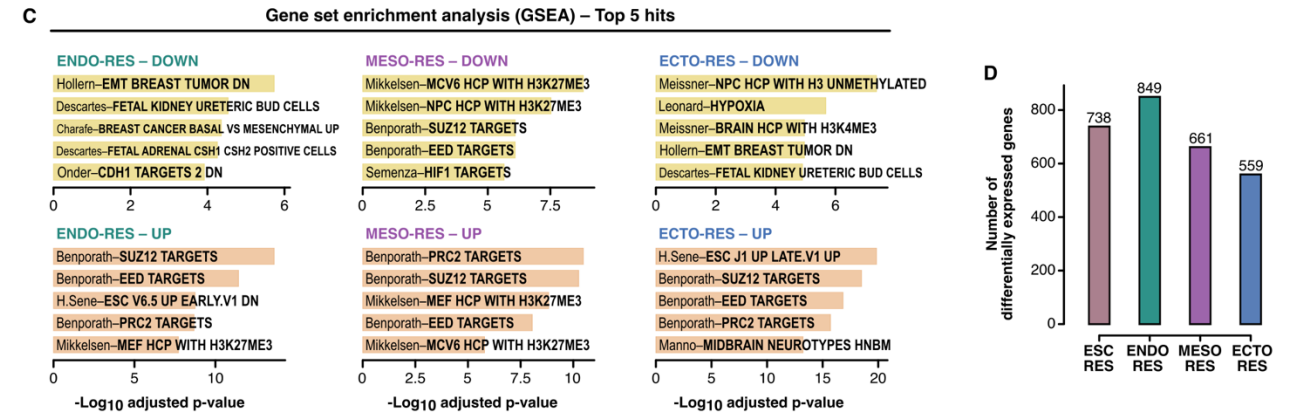
C
Gene set enrichment analysis (GSEA) – Top 5 hits
ENDO-RES – DOWN
Hollern–EMT BREAST TUMOR DN
Descartes–FETAL KIDNEY URETERIC BUD CELLS
Charafe–BREAST CANCER BASAL VS MESENCHYMAL UP
Descartes–FETAL ADRENAL CSH1 CSH2 POSITIVE CELLS
Onder–CDH1 TARGETS 2 DN
MESO-RES – DOWN
Mikkelsen–MCV6 HCP WITH H3K27ME3
Mikkelsen–NPC HCP WITH H3K27ME3
Benporath–SUZ12 TARGETS
Benporath–EED TARGETS
Semenza–HIF1 TARGETS
ECTO-RES – DOWN
Meissner–NPC HCP WITH H3 UNMETHYLATED
Leonard–HYPOXIA
Meissner–BRAIN HCP WITH H3K4ME3
Hollern–EMT BREAST TUMOR DN
Descartes–FETAL KIDNEY URETERIC BUD CELLS
ENDO-RES – UP
Benporath–SUZ12 TARGETS
Benporath–EED TARGETS
H.Sene–ESC V6.5 UP EARLY.V1 DN
Benporath–PRC2 TARGETS
Mikkelsen–MEF HCP WITH H3K27ME3
MESO-RES – UP
Benporath–PRC2 TARGETS
Benporath–SUZ12 TARGETS
Mikkelsen–MEF HCP WITH H3K27ME3
Benporath–EED TARGETS
Mikkelsen–MCV6 HCP WITH H3K27ME3
ECTO-RES – UP
H.Sene–ESC J1 UP LATE.V1 UP
Benporath–SUZ12 TARGETS
Benporath–EED TARGETS
Benporath–PRC2 TARGETS
Manno–MIDBRAIN NEUROTYPES HNBM
-Log10 adjusted p-value

D
Number of differentially expressed genes
738
849
661
559
ESC RES
ENDO RES
MESO RES
ECTO RES

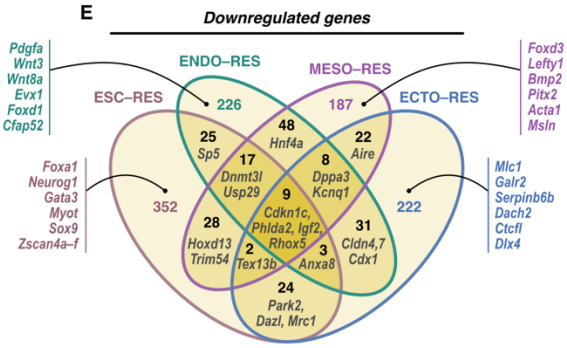
E
Downregulated genes
ESC–RES
ENDO–RES
MESO–RES
ECTO–RES
Pdgfa Wnt3 Wnt8a Evx1 Foxd1 Cfap52
Foxd3 Lefty1 Bmp2 Pitx2 Acta1 Msln
Foxa1 Neurog1 Gata3 Myot Sox9 Zscan4a–f
Mlc1 Galr2 Serpinb6b Dach2 Ctcfl Dlx4
352
226
187
222
25 Sp5
48 Hnf4a
22 Aire
17 Dnmt3l Usp29
8 Dppa3 Kcnq1
9 Cdkn1c, Phlda2, Igf2, Rhox5
28 Hoxd13 Trim54
2 Tex13b
3 Anxa8
31 Cldn4,7 Cdx1
24 Park2, Dazl, Mrc1

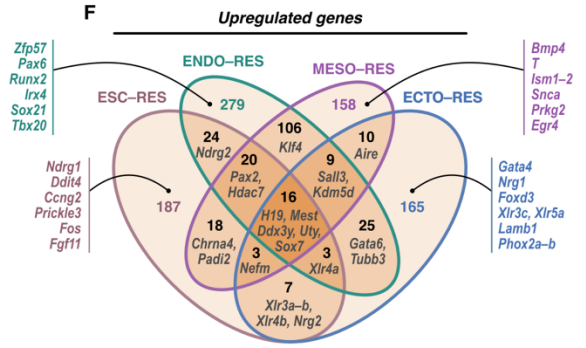
F
Upregulated genes
ESC–RES
ENDO–RES
MESO–RES
ECTO–RES
Zfp57 Pax6 Runx2 Irx4 Sox21 Tbx20
Bmp4 T Ism1–2 Snca Prkg2 Egr4
Ndrg1 Ddit4 Ccng2 Prickle3 Fos Fgf11
Gata4 Nrg1 Foxd3 Xlr3c, Xlr5a Lamb1 Phox2a–b
279
158
187
165
24 Ndrg2
106 Klf4
10 Aire
20 Pax2, Hdac7
9 Sall3, Kdm5d
16 H19, Mest Ddx3y, Uty, Sox7
18 Chrna4, Padi2
25 Gata6, Tubb3
3 Nefm
3 Xlr4a
7 Xlr3a–b, Xlr4b, Nrg2

Figure 7: Lasting effects on gene expression patterns upon differentiation to germ layers. **(A)** Schematic diagram depicting *Dnmt1*^{CTL} and *Dnmt1*^{RES} derived germ layer cell types. **(B)** Differential gene expression in *Dnmt1*^{RES} versus *Dnmt1*^{CTL} endoderm, mesoderm and ectoderm determined by an adjusted p-value ≤ 0.05 and $\log_2$ fold change ≤ -0.6 or ≥ 0.6 using mRNA sequencing analyzed with the DESeq2 software. **(C)** Gene set enrichment analysis for down- and upregulated genes in *Dnmt1*^{RES} germ layers. **(D)** Total number of differentially expressed genes in *Dnmt1*^{RES} cell types. **(E-F)** Overlap of downregulated and upregulated genes, respectively, among *Dnmt1*^{RES} cell types. See also Table S6 and Figure S7.

We then proceeded with gene set enrichment analysis (GSEA) of down- and upregulated genes in *Dnmt1*^{INV} and *Dnmt1*^{RES}, selecting their top 10 significantly enriched gene sets (Figure 6D). EED[74], SUZ12[74], PRC2[74], and KDM1A[75] targets stood out among upregulated gene sets in *Dnmt1*^{INV}, and, interestingly, EED and SUZ12 targets were conversely enriched in *Dnmt1*^{RES} downregulated genes. PRC2, comprising SUZ12 and EED among its components, mediates the deposition of H3K27me3 in bivalent developmental gene promoters[76]. Nearly all promoters of dysregulated PRC2/SUZ12/EED target genes[74] (non-redundant: n=547) exhibited a simultaneous sharp surge in H3K4me3 and decline in H3K27me3 centered at their TSS in *Dnmt1*^{INV}, with levels returning to baseline in *Dnmt1*^{RES} (Figure 6E). This temporary transition to an active chromatin state occurred independently of changes in CpG methylation levels within TSS regions, which remained consistently very low across all conditions (median levels < 5.5%), and independently of gene expression dysregulation patterns (Figure S6D; Table S7), as exemplified by epigenetic profiles of *Fos* and *Nkx2-9* (Figure 6F). Additional compelling insights emerged from our GSEA analysis. Pluripotency network[77], embryonic stem cell core[78], MYC targets[79], and CHEK2 network[80] gene sets were enriched among *Dnmt1*^{INV} downregulated genes, while *Dnmt1*^{RES} upregulated genes showed predominant enrichment in hypoxia gene sets[79,81-85], suggesting disturbances in potency, cell cycle regulation, and cellular stress responses. In fact, we observed permanently slower cell proliferation (Figure 6G) and dynamic changes in cell size and internal complexity (i.e. granularity) (Figures 6H-I and S7A), possibly signaling altered potency state transitions and cell cycle dynamics. Signs of genomic instability were also evident, including a latent increase in DNA damage measured by the presence of γH2AX (Figures 6J and S7A) and permanent telomere shortening (Figure 6K), indicative of cellular stress.

The observed molecular and cellular dysfunction prompted us to investigate how temporary inactivation of *Dnmt1* in mESCs would impact gene expression upon differentiation. *Dnmt1*^{CTL} and *Dnmt1*^{RES} mESCs were differentiated into endoderm, mesoderm, and ectoderm germ layers (Figure 7A) which were sorted based on lineage-specific cell surface markers and viability to obtain pure live populations, circumventing gene expression alterations linked to cell fixation or apoptosis. Similar percentages of marker-positive cells were obtained in *Dnmt1*^{CTL} and *Dnmt1*^{RES} derived lineages (Figure S7B), and gene expression principal component analysis showed clear clustering among cell types and conditions (Figure S7C). *Dnmt1*^{CTL} and *Dnmt1*^{RES} ectoderm inductions were similarly successful; compared to mESCs, pluripotency markers were markedly lower and differentiation markers were markedly higher, whereas differences between *Dnmt1*^{CTL} and *Dnmt1*^{RES} inductions were noticeable for endoderm and mesoderm (Figure S7D-F). Differential gene expression analysis in *Dnmt1*^{RES} versus *Dnmt1*^{CTL} derived germ layers revealed hundreds of dysregulated genes (Figure 7B; Table S6), compellingly showing enrichment for PRC2[74], SUZ12[74] and EED[74] targets (Figure 7C) as was observed in mESCs (Figure 6D). Among *Dnmt1*^{RES} cell types, endoderm had the highest number of dysregulated genes, followed by mESCs, mesoderm, and ectoderm (Figure 7D). Interestingly, down- and upregulated genes in *Dnmt1*^{RES} cell types were primarily cell type-specific, though some were shared among multiple *Dnmt1*^{RES} cell types such as *Dnmt3l* downregulated in mESCs, endoderm and mesoderm, and *Sall3* upregulated in all germ layers (Figures 7E-F).

In summary, lack of sustained DNA methylation maintenance by *Dnmt1* in mESCs induced persistent epigenomic and genomic instability, cellular dysfunction, and gene expression dysregulation, leading to lineage-specific effects emerging upon differentiation into germ layers.

DISCUSSION

In this study, *Dnmt1* inactivation and rescue in mESCs led to extensive remodelling of DNA methylation, histone modifications and gene expression and had a transformative impact on genomic stability, transposable element silencing, cellular processes, and differentiation.

Mouse ESC and embryo models remain invaluable tools for uncovering novel imprinted regions through disruption of genomic imprinting maintenance. However, characterization of imprints is highly complex due to diverse regulatory factors and epigenetic modifications, often defying a universal paradigm. Consequently, studies typically target a single mechanism of genomic imprinting maintenance for subsequent detailed examination, aligning with our study's focus on DNMT1. Consolidating results from various studies is therefore imperative for reconciling the multiple layers of genomic imprinting regulation. Indeed, integrating public datasets into our methodology facilitated the identification of regions with gDMR-like properties and strengthened the validity of these regions, while reciprocally supporting previous work. Cross-validation is also critical to mitigate biological discrepancies or epigenomic sequencing limitations. For instance, ICRs and gDMRs do not consistently display anticipated epigenetic signatures in control conditions across various model systems, as was observed in our data where only 15 out of 26 ICRs and gDMRs showed substantial DNA methylation levels within broad H3K9me3 domains in *Dnmt1*^{CTL}. Such inconsistencies were also evident in mouse gamete CpG methylation data from Wang et al.[63] where the *Meg3* ICR did not exhibit expected sperm-specificity and in data from Shi et al.[35] where ZFP57 binding sites in mESCs only overlapped 11 out of the 20 ICRs that were screened. In recent work by Yang et al.[86], genomic regions with imprinted signatures were identified in mouse preimplantation embryos through allele-specific profiling of DNA methylation and H3K9me3 alongside global depletion of H3K9me3 to establish mechanistic co-dependency. Yet, their analysis yielded only 19 known ICRs among identified regions. Nonetheless, they unveiled 22 ICR-like regions and performed Cas9-mediated deletions of five, demonstrating their importance for mouse development. Compellingly, three of our gDMR-like regions—*Spred2*, *Lipt1-Mitd1* and *Zfp668*—coincided with ICR-like regions identified by Yang et al., with *Lipt1-Mitd1* among the five that were confirmed biologically relevant. *LIPT1* is the causative gene for lipoyltransferase 1 deficiency in humans, a rare inborn metabolism disorder with which *MITD1* is also associated[87-90], and *SPRED2* for Noonan syndrome 14[91], a severe developmental disorder. Other gDMR-like regions uncovered in our study are associated with genes implicated in human diseases, such as *REPIN1* linked to non-alcoholic fatty liver disease[92] and polycystic ovary syndrome[93], *HCN2* to epilepsy[94-97], *RNF216* to cerebellar ataxia-hypogonadism syndrome[98,99] and *VSIG10* to COVID-19[100]. In our model, these genes showed dysregulated expression linked to de-repression of their gDMR-like region, thus further investigation into the functionality of these regions may unveil novel disease associations.

While DNA methylation and H3K9me3 are extensively investigated in genomic imprinting, cellular and animal mouse studies have implicated additional histone modifications. Imprinted (i.e. repressed) alleles, co-marked by DNA methylation and H3K9me3[34,40,86,101], may occasionally also display H3K27me3[40,101], whereas H3K4me2/3[40,101,102] and H3K27ac[103] characterize permissive alleles, which can exhibit bivalency with concurrent H3K27me3[40,101,102]. Our study was distinctive for simultaneously profiling H3K4me3, H3K4me1, H3K27ac and H3K27me3, alongside customary DNA methylation and H3K9me3, offering an unprecedented perspective on the complex and divergent nature of imprinting mechanisms. While de-repression (i.e. DNA hypomethylation and decreased H3K9me3) of ICRs, gDMRs, and gDMR-like regions following *Dnmt1* inactivation resulted in widespread increase in H3K4me3 and H3K4me1, we observed variable fluctuations in H3K27ac and H3K27me3. Interestingly, in certain instances, overlapping increases in H3K4me3/H3K4me1 and H3K27ac/H3K27me3 were detected, a perplexing phenomenon as these pairs occur on the same amino acid rendering them mutually exclusive. However, asymmetrical nucleosome modification[104] or cellular heterogeneity could account for this observation. Additionally, epigenetic cross-talk between alleles known as transvection[105-108] could suggest differential allelic effects, warranting further investigation using a model that allows for robust allele-specific profiling of epigenetic marks and chromatin interactions. Until now, the role of H3K4me1 in genomic imprinting has remained unexplored, but its correlation with enhancer activity[109-112] imputes relevance for permissiveness of

imprinted loci, a notion supported by our findings. H3K4me1 can help distinguish promoter versus enhancer activity, and active versus poised states, valuable regulatory nuances for elucidating imprinting mechanisms.

Beyond genomic imprinting maintenance, DNMT1 preserves DNA methylation patterns and genomic stability during cell division. In the S phase of the cell cycle, DNMT1 methylates newly synthesized DNA through its interaction with proliferating cell nuclear antigen (PCNA)[113,114] and restores methylation following DNA repair[12]. Stressful conditions such as viral infection[115], inflammation[116] or DNA hypomethylation due to DNMT1 depletion[117] can induce cell cycle arrest in G1 to prevent DNA damage accumulation in S phase. Progression to S phase despite stress can increase DNA damage and trigger the G2/M checkpoint for G2 arrest[118,119]. In our study, *Dnmt1* inactivation led to downregulation of *Ccnd1/2*, essential for G1/S transition[120-123], whereas *Ccng2*, implicated in G1 and G2 arrest[124-127], was upregulated after *Dnmt1* rescue alongside increased DNA damage. We thus speculate that reduction of cell proliferation observed in both conditions was linked to cell cycle arrest, in G1 for *Dnmt1**INV*** due to drastic epigenomic remodelling and in either G1 or G2 for *Dnmt1**RES***. Less severe epigenomic changes in *Dnmt1**RES*** could have allowed some cells to escape G1 arrest, culminating in DNA damage accumulation and G2/M checkpoint activation. Given that cell cultures remained viable, cell cycle arrest was likely unsynchronized, occurring transiently or permanently in a subset of cells. Another indication of cell cycle arrest in *Dnmt1**INV*** and *Dnmt1**RES*** was telomere shortening[128-130], possibly linked to permanent downregulation of *Zscan4a-f*[71] and *Tcstv3*[72], required for telomere elongation in mESCs. Moreover, *Zscan4a-f* and *Tcstv3* are part of a mouse 2-cell embryo (2C) gene network activated in rare mESC subpopulations as they cycle in and out of a 2C-like totipotent state[69,70]. This 2C-like totipotent state is further characterized by decreased DNA methylation levels, absence of pluripotency marker OCT4/POU5F1, upregulation of MERVL and MT2 LTRs and generation of MERVL- and MT2-derived chimeric gene transcripts[69,70]. Our study showed that *Dnmt1* inactivation and rescue in mESCs permanently upregulated MERVL and MT2 transcripts associated with their DNA hypomethylation and provided evidence suggesting associated gene transcript chimerism. Conversely, Eckersley-Maslin et al. did not observe MERVL upregulation upon *Dnmt1* repression in mESCs[70]. However, they repressed *Dnmt1* for only three days, after which mean whole-genome and MERVL-specific DNA methylation dropped to ~30%, in contrast to six days of *Dnmt1* repression in our study, where mean levels dropped to ~3.5% and ~3.2%, respectively. Three days of *Dnmt1* repression was possibly insufficient for MERVL upregulation. In our model, permanent upregulation of MERVL and MT2 and downregulation of *Zscan4a-f* and *Tcstv3* alongside stable *Pou5f1* expression could indicate atypical potency state transitions in *Dnmt1**RES*** mESCs, potentially compromising proper differentiation processes and cell-fate decisions. We demonstrated that germ layers derived from *Dnmt1**RES*** mESCs displayed lineage-specific and pan-lineage gene expression alterations, affecting endoderm and mesoderm with greater severity compared to ectoderm. Downregulation of *Dnmt3l* in *Dnmt1**RES*** mESCs persisting only in endoderm and mesoderm could have instigated deviations in their differentiation trajectories, as DNMT3L is a crucial co-factor for DNMT3A-mediated *de novo* DNA methylation[131,132], essential for orchestrating mammalian embryonic development[133]. Upregulation of *Sall3* in all *Dnmt1**RES*** germ layers may have also contributed to lineage-specific effects. In human induced pluripotent stem cells, SALL3 serves as a predictive marker for differentiation propensity, positively correlating with ectoderm and negatively with endoderm/mesoderm, mechanistically via modulation of DNMT3B function[134], another vital *de novo* DNA methyltransferase[133]. Gene expression regulation may have been supported by *Sall3* upregulation in *Dnmt1**RES*** ectoderm, while being hindered in *Dnmt1**RES*** endoderm and mesoderm.

In conclusion, this study demonstrates the necessity of sustained DNMT1-mediated DNA methylation maintenance in mESCs for safeguarding epigenomic and genomic stability, transposable element silencing and cellular functions, and contributes to the ongoing search for novel imprinted regions. By revealing molecular and cellular transformations arising from a transient epigenetic perturbation in mESCs, we emphasize the broader implications of epigenetic regulators and offer cautionary insights into their modulation. These findings provide valuable perspectives for conducting epigenetic interventions, unraveling pathophysiological mechanisms, and understanding the long-term impact of epigenetic stress during early embryonic development.

LIMITATIONS OF THE STUDY

This study presents some limitations that warrant consideration. Firstly, EM-seq does not distinguish 5-methylcytosine (5mC; methylation) from 5-hydroxymethylcytosine (5hmC; hydroxymethylation), an intermediate product of DNA demethylation by TET enzymes. However, given the low global 5hmC levels in mESCs (~3%)[135] and the stable expression of *Tet1-3* in our model, it is unlikely that 5hmC substantially skewed our results. Moreover, lack of parental single nucleotide polymorphisms in *Dnmt1*$^{tet/tet}$ mESCs prevented robust allele-specific profiling of epigenetic modifications and gene expression, thereby constraining the depth of our investigation into genomic imprinting maintenance. Additionally, while *Dnmt1* expression was shown to be higher in *Dnmt1*$^{tet/tet}$ mESCs compared to WT[29,136,137], this variation was outweighed by the superior efficiency of the Tet-Off system in transiently inactivating *Dnmt1* across entire cell populations compared to alternative methods such as DNMT1 inhibitors (e.g. 5-azacytidine[138], decitabine[139], GSK-3484862[139,140]) or siRNA interference[141], the former also lacking specificity and inducing cytotoxicity. Lastly, male mESCs were chosen to avoid X inactivation effects and enable analysis of both sex chromosomes, but generating a female cell line could enhance our understanding of sex-specific responses to epigenetic perturbations.

ACKNOWLEDGEMENTS

We thank the members of the McGraw laboratory for valuable insights and support throughout the course of this study, the McGill Genome Centre and *Génome Québec* for sequencing services, Ines Boufaied for assisting with FACS assays, as well as Gregor Andelfinger and Richard Chaillet for gifting R1 and *Dnmt1*$^{tet/tet}$ mESCs, respectively. This work was supported by a Natural Sciences and Engineering Research Council of Canada grant to S.M. and scholarship to E.E., a *Réseau Québecois en Reproduction* grant to S.M. and N.G., and a FRQS-Junior 2 salary award to S.M. The graphical abstract and Figures 1A and 7A were created with BioRender.com.

AUTHOR CONTRIBUTIONS

Conceptualization & methodology: E.E., S.M., V.B.L., T.D., N.R., N.G., G.B., D.S.; Investigation: E.E., L.M.L.; Formal analysis: E.E., A.L., M.C.; Writing–original draft: E.E., S.M.; Writing–review & editing: All authors; Visualization: E.E.; Supervision: S.M., G.B., D.S.; Funding acquisition: S.M., N.G.

DECLARATION OF INTEREST

The authors declare no competing interests.

SUPPLEMENTAL INFORMATION

Figures S1-7 are included in the supplemental file “Supplemental Figures (Elder et al 2024 PREPRINT).pdf”

Tables S1-7 are included in the supplemental file “Supplemental Tables (Elder et al 2024 PREPRINT).xlsx”

Table S1: Association of permanent CpG hypomethylation with genomic locations.
Related to Figures 3 and S2.

Table S2: Association of permanent CpG hypomethylation with histone modification remodulation.
Related to Figures 3 and S2.

Table S3: Epigenetic landscapes of ICRs, gDMRs and gDMR-like regions.
Related to Figures 4 and S3.

Table S4: Differential expression of genes associated with ICRs, gDMRs and gDMR-like regions.
Related to Figure S4.

Table S5: CpG methylation and transcript levels of MERVL-int and MT2_Mm loci.
Related to Figure 5.

Table S6: Dysregulated gene lists for mESCs, endoderm, mesoderm, and ectoderm.
Related to Figures 6, 7 and S6.

Table S7: Non-redundant PRC2/SUZ12/EED targets with gene expression dysregulation in mESCs.
Related to Figures 6 and S6.

DATA AND CODE AVAILABILITY

Raw and processed data will be made publicly available once this study is in press. This study does not report original code. However, scripts for data analysis and visualization can be provided upon request to lead contact.

METHODOLOGY

Cell lines and culture protocol

R1 and *Dnmt1*$^{tet/tet}$ mESCs were gifted by Gregor Andelfinger and Richard Chaillet, respectively. Both cell lines were maintained on gelatin-coated plates, free of mouse embryonic fibroblast feeder cells, in mESC culture medium in humidified atmosphere with 5% CO_2 at 37 °C. Cell culture plates were coated with 0.1% solution of gelatin (Sigma-Aldrich, G1890) in DPBS 1X (Corning, 21-031-CV), then placed in the incubator for 30 minutes after which excess gelatin was removed. Culture medium for mESCs consisted of DMEM (Corning, 10-013-CV) supplemented with 15% ES cell qualified fetal bovine serum (Thermo Fisher, 16141079), 1% 2-mercaptoethanol 100X (Sigma-Aldrich, ES-007-E), 1% non-essential amino acids 100X (Thermo Fisher, 11140050), 1% L-Glutamine 200 mM (Corning, 25-005-CI), 1% nucleosides 100X (Sigma-Aldrich, ES-008-D), 1% penicillin-streptomycin 100X (Corning, 30-002-CI) and 10^3 units/mL of recombinant mouse LIF protein (Sigma-Aldrich, ESG1107), which was stored at 4 °C for up to 1 week. Culture medium was changed every day and cell confluency was maintained below 80%. Trypsin-EDTA 0.25% (Thermo Fisher, 25200056) was used for passaging cell cultures, typically every other day. *Dnmt1*$^{tet/tet}$ mESCs were authenticated by Richard Chaillet's laboratory members who developed and published this cell line[29]. R1 mESCs were not formally authenticated as they were only used as the reference DNA sample for relativizing telomere length measurements in *Dnmt1*$^{tet/tet}$ mESCs.

Dnmt1 inactivation and rescue in *Dnmt1*$^{tet/tet}$ mESCs

To inactivate *Dnmt1*, *Dnmt1*$^{tet/tet}$ mESCs were treated with 2 µg/mL doxycycline hyclate (Sigma-Aldrich, D9891), a tetracycline derivative, which was added to the culture medium for 6 days. Then, doxycycline treatment was stopped, and cells were maintained for 21 days. Samples were collected prior to doxycycline treatment (*Dnmt1* control), immediately following doxycycline treatment (*Dnmt1* inactive), and after the 21-day period of recovery from doxycycline treatment (*Dnmt1* rescue).

Genomic region annotations

Genomic coordinates for ICRs and gDMRs were curated from literature[38-61], sources specific to each ICR and gDMR are listed in Table S3. Allele-specific methylated regions in mESCs identified by the Smith Lab[62] in data from Leung et al.[34] were obtained using the UCSC table browser[142]. Rsubread[143] v2.16.1 was used to obtain gene transcription start sites (TSS), TSS regions (+/- 200 bp from TSS), promoters (-2000 and +200 bp from TSS), and gene bodies. Genomic regions not within promoters or gene bodies were considered as intergenic. Annotatr[144] v1.28.0 was used to obtain CpG islands, CpG island shores (+/- 2kb from CpG islands) and CpG island shelves (+/- 2kb from CpG island shores). Genomic regions not within CpG islands, CpG island shores or CpG island shelves were considered as open sea. Using the UCSC table browser[142], CTCF-bound candidate cis-regulatory elements (cCREs) were extracted from the ENCODE Registry of cCREs[145] filtering for CTCF-only_CTCF-bound, PLS_CTCF-bound, dELS_CTCF-bound, pELS_CTCF-bound and DNase-H3K4me3_CTCF-bound ENCODE classifications. LINEs, SINEs and LTRs were extracted from RepeatMasker using the UCSC table browser[142]. The mouse reference genome assembly GRCm38/mm10 was used for generating all annotations.

Enzymatic methyl sequencing and data analysis

The following steps were performed in triplicates for each experimental condition: genomic DNA extraction using the QIAamp DNA Mini Kit (QIAGEN, 51304), library preparation using the NEBNext® Enzymatic Methyl-seq Kit (New England Biolabs, E7120L) and 150 bp paired-end sequencing using the Illumina NovaSeq 6000 technology. Library preparation and sequencing was conducted by *Génome Québec*. Between 291M and 385M raw reads were obtained per sample.

Raw reads were processed using the GenPipes[146] methylation sequencing pipeline v3.6.0. Trimmomatic[147] v0.36 was employed for quality trimming of raw reads and removal of sequencing adapters, Bismark[148] v0.18.1 for read alignment to the mouse reference genome assembly GRCm38/mm10, Sambamba[149] v0.7.0 for merging read set files of each sample, Picard v2.9.0 for removing duplicate reads and the methylation extractor function from Bismark[148] v0.18.1 for obtaining the methylation level of single CpGs. Only CpGs that were sequenced in all samples with a coverage ≥ 10X were retained. Methylation levels of single CpGs were then averaged across triplicate samples for each experimental condition.

CpGs were annotated to genomic regions of interest using annotatr[144] v1.28.0. Annotation to promoters was given priority over gene bodies and CpG islands were prioritized over CpG island shores and shelves, with shores taking precedence over shelves. For annotation to transposable elements, only LINEs, SINEs and LTRs with a Smith Waterman alignment score ≥ 1000 were considered. When conducting differential analysis among experimental conditions, we used a 20% change in methylation levels of single CpGs and a 10% change in mean methylation levels across a specific genomic region as thresholds for establishing significance. For comparisons involving groups of multiple CpGs or genomic regions, appropriate statistical testing was applied as described in the quantification and statistical analysis section.

Chromatin immunoprecipitation sequencing and data analysis

Chromatin immunoprecipitation (ChIP) sequencing was performed in duplicates for each histone modification per experimental condition and one aliquot of non-immunoprecipitated chromatin (i.e. input) was sequenced per experimental condition. First, cells were fixed with a solution consisting of 13% formaldehyde (Sigma-Aldrich, 47608) in DPBS (Corning, 21-031-CV) for 10 minutes at room temperature with gentle rocking. Then, cell and nuclei lysis was performed, and chromatin was purified and sonicated using buffers and protocols from the IDeal ChIP-Seq Histone Kit (Diagenode, C01010051). Sonication was conducted with the Bioruptor® Pico sonication device (Diagenode, B01060010) for 15 cycles (30 seconds ON/ 30 seconds OFF) to obtain DNA fragments

between 150-400bp. Next, chromatin was pre-cleared via incubation with protein G Dynabeads™ (Thermo Fisher, 10009D) for 1h at 4°C on a rotator, after which samples were placed on a magnetic rack and input aliquots were taken from the supernatant. Chromatin immunoprecipitation was then conducted as follows. Pre-cleared chromatin samples were incubated overnight at 4°C on a rotator with histone modification antibodies–either anti-H3K4me3 (Active Motif, 39159), anti-H3K27ac (Abcam, ab4729), anti-H3K4me1 (Cell signaling technology, 5326), anti-H3K27me3 (Sigma-Aldrich, 07-449) or anti-H3K9me3 (Abcam, ab8898)–in quantities recommended by the antibody manufacturer. Dynabeads™ were added to the chromatin-antibody mixtures and were incubated for an additional 2h at 4°C on a rotator. Protein A Dynabeads™ (Thermo Fisher, 10001D) or protein G Dynabeads™ (Thermo Fisher, 10009D) were used depending on the antibody source. Washing, elution, decrosslinking and DNA purification were then conducted using the IDeal ChIP-Seq Histone Kit (Diagenode, C01010051). Finally, libraries were prepared with the KAPA HyperPrep Kit (Roche, KK8502) and 50 bp paired-end sequencing was performed at the McGill Genome Centre using the Illumina HiSeq® 2500 technology. Between 16M and 59M raw reads were obtained per sample.

Raw reads were processed using a homemade pipeline including Trimmomatic[147] v0.32 for quality trimming of raw reads and removal of sequencing adapters, Burrows-Wheeler Aligner[150] v0.6.1 for read alignment to the mouse reference genome assembly GRCm38/mm10, the MergeSamFiles.jar and MarkDuplicates.jar scripts from Picard v1.70 for merging read set files of each sample and removing duplicate reads, respectively, and the View function from SAMtools[151] v0.1.18 for filtering reads as to only retain those with a MAPQ score ≥ 15. Then, peak calling was performed using MACS2[152] v2.0.10 with Python v2.7.8, correcting background noise with input signals. Next, MACS2 outputs and BAM files converted to BED format (via the bamTobed function from BEDTools[153] v2.27) were used in the profile_bins function from MAnorm2_utils v1.0.0. The profile_bins function allowed for genomic regions of MACS2 called peaks to be merged into a common set of histone-modified regions across all samples for each histone modification, computing normalized signal enrichment within each region. Finally, MAnorm2[154] v1.0.0 was employed for conducting differential analysis of enrichment signals between experimental conditions, providing a p-value and $\log_2$ fold change for each histone-modified region. Annotatr[144] v1.28.0 was used to overlap histone-modified regions with other genomic regions and for measuring histone modification RPKM levels within specific regions of interest. Visualization of RPKM signal enrichment within specific target regions in Figure 6E were generated with ComplexHeatmap[155] v2.16.0 and EnrichedHeatmap[156] v1.30.0.

Mouse sperm and oocyte CpG methylation

Mouse sperm and oocyte CpG methylation profiles were produced by Wang et al.[63] and analyzed by the Smith Lab[62] using the mouse reference genome assembly GRCm38/mm10. These were obtained via the UCSC table browser[142] and annotated to genomic regions of interest using annotatr[144] v1.28.0 after which mean sperm- and oocyte-specific levels were computed.

ZFP57 DNA binding motif enrichment analysis

The ZFP57 DNA binding motif MA1583.1[157,158] was obtained from the JASPAR database[159]. Enrichment analysis was conducted using the Simple Enrichment Analysis (SEA) tool from the MEME Suite[160] v5.5.5 with shuffled input sequences used as controls.

mRNA sequencing and data analysis

mRNA sequencing was conducted in triplicates for all experimental conditions. RNA was extracted using the RNeasy Mini Kit (QIAGEN, 74104), libraries were prepared with the NEBNext® Ultra™ II Directional RNA Library Prep Kit (New England Biolabs, E7765) in conjunction with the NEBNext® Poly(A) mRNA Magnetic Isolation Module (New England Biolabs, E7490) and 100 bp paired-end sequencing was performed with the Illumina

NovaSeq 6000 technology. Library preparation and sequencing was conducted by *Génome Québec*. Between 27M and 53M raw reads were obtained per sample.

Raw reads were processed using the GenPipes[146] RNA sequencing pipeline v3.1.4. First, Trimmomatic[147] v0.36 was used for quality trimming of raw reads and removal of sequencing adapters and STAR[161] v2.5.3a was used for aligning reads to the mouse reference genome assembly GRCm38/mm10. Then, several functions from Picard v2.9.0 were employed: MergeSamFiles for merging read alignment files of each sample, SortSam for sorting files by coordinate and MarkDuplicates for identifying read duplicates. Next, the HTSeq_count function from HTSeq[162] v0.7.2 was used with Python v2.7.13 for calculating raw counts and StringTie[163] v1.3.5 was used for transcript assembly. Finally, DESeq2[164] v1.18.1 was used with R v3.4.3 for generating normalized counts and conducting differential gene expression analysis between experimental conditions, producing an adjusted p-value and $\log_2$ fold change for each gene.

RNA sequencing and data analysis for transposable elements

RNA sequencing was conducted in duplicates for all experimental conditions. The AllPrep DNA/RNA Mini Kit (QIAGEN, 80204) was used for RNA extraction and the TruSeq® Stranded Total RNA Library Prep Human/Mouse/Rat Kit (Illumina, 20020596) for library preparation. 75 bp paired-end sequencing was then performed at the McGill Genome Centre with the Illumina HiSeq® 4000 technology. Between 63M and 88M raw reads were obtained per sample.

Raw reads were processed using the GenPipes[146] RNA sequencing pipeline v3.1.4. First, Trimmomatic[147] v0.36 was used for quality trimming of raw reads and removal of sequencing adapters and then reads were aligned to the mouse reference genome assembly GRCm38/mm10 using STAR[161] v2.5.3a. Next, several functions from Picard v2.9.0 were employed including MergeSamFiles for merging read alignment files of each sample, SortSam for sorting files by coordinate and MarkDuplicates for identifying read duplicates. Then, we incorporated the featureCounts[165] function from Subread[166] v2.0.6 to obtain raw counts corresponding to genomic regions of LINE, SINE, and LTR elements, extracted from RepeatMasker using the UCSC table browser[142]. Finally, we employed DESeq2[164] v1.18.1 with R v3.4.3 to generate normalized counts for each element, which were then averaged across replicates for each experimental condition.

LINEs, SINEs and LTRs were then filtered based on their Smith Waterman alignment score, only retaining those with a score ≥ 1000 for downstream transcriptional analysis. When comparing total normalized counts of an element between experimental conditions, a $\log_2$ fold change ≤ -1 or ≥ 1 was used as a threshold for establishing significance. For comparisons involving grouped locus-specific normalized counts, appropriate statistical testing was applied as described in the quantification and statistical analysis section.

Gene set enrichment analysis

Gene set enrichment analysis (GSEA) was conducted using the enricher function from clusterProfiler[167] v4.8.2. All gene sets available for Mus musculus in the Molecular Signatures Database[79,168] were extracted via msigdbr v7.5.1. The following parameters were applied for the GSEA: Benjamini–Hochberg p-value adjustment, minimum gene set size of 10 and maximum gene set size of 1000.

Visualization of genomic signal tracks

Genomic signal track figures were generated with Gviz[169] v1.44.2. Signal tracks of sample replicates were merged by computing their average signals within common 10-bp bins using the banCoverage function from deepTools[170] v3.5.2, with forward and reverse tracks for RNA-seq and mRNA-seq being priorly merged for each sample. Signal

tracks for *Zfp57* WT and KO mESCs were produced by Shi et al.[35] and for *Setdb1* WT and KO mESCs by Barral et al.[64], which were obtained via the Gene Expression Omnibus[171,172].

FACS assay for detecting γH2AX and assessing cell size and granularity

The H2AX phosphorylation (γH2AX) for fluorescence-activated cell sorting (FACS) kit (Sigma-Aldrich, 17-344) was used to prepare cell samples following the manufacturer's protocol for fixation, permeabilization and staining. All experimental conditions were assayed in triplicates for γH2AX, and one unstained control sample was included per condition. One DNA damage positive control sample stained for γH2AX was also included, which consisted of *Dnmt1*^{CTL} mESCs that were irradiated with 10 Gγ using a Faxitron® irradiator six days prior to sorting. Samples were sorted with the BD LSRFortessa™ Cell Analyzer (BD Biosciences) and data was processed with the BD FACSDiva™ software v8.0.2. Forward scatter area (FSC-A) and side-scatter area (SSC-A) measurements were used for filtering out apoptotic-like cells prior to fluorescence analysis. FSC-A and SSC-A measurements of live cell populations were then used for assessing cell size and granularity, respectively.

Measuring relative telomere length by qPCR

Genomic DNA was extracted from *Dnmt1*$^{tet/tet}$ mESCs and R1 mESCs using the QIAamp DNA Mini Kit (QIAGEN, 51304). qPCR primer sequences for mouse telomeric and *Rplp0* (single-copy gene) DNA were obtained from Callicott & Womack[173], who adapted the protocol developed by Cawthon[174] for measuring relative telomere length in human samples. qPCR primers were ordered from Integrated DNA Technologies and evaluated using customary PCR techniques, including annealing temperature optimization and amplification efficiency assessment. qPCR assays were performed using a LightCycler® 480 instrument (Roche) and the SensiFAST™ SYBR® No-ROX Kit (Bioline, BIO-98005), following the kit's 3-step protocol for 30 cycles with an annealing temperature of 62 °C. Telomeric and *Rplp0* DNA were amplified by qPCR in all *Dnmt1*$^{tet/tet}$ mESC conditions and in R1 mESCs, with eight replicates for each amplification to ensure reproducibility. For telomeric DNA amplifications, 0.2 ng of DNA was used and for *Rplp0* DNA amplifications, 2 ng of DNA was used. Relative telomere length was calculated for individual replicates of each *Dnmt1*$^{tet/tet}$ mESC condition with the delta-delta Ct method[175] as in the protocol by Cawthon, using *Rplp0* as the reference single-copy gene for normalization and R1 mESCs as the reference DNA sample for relativization. The average *Rplp0* Ct value for each condition was used for normalizing telomeric DNA Ct values and the average normalized telomeric DNA Ct value in R1 mESCs was used for relativizing telomere length measurements in *Dnmt1*$^{tet/tet}$ mESCs.

Mouse telomeric DNA forward qPCR Primer:
CGGTTTGTTTGGGTTTGGGTTTGGGTTTGGGTTTGGGTT

Mouse telomeric DNA reverse qPCR Primer:
GGCTTGCCTTACCCTTACCCTTACCCTTACCCTTACCCT

Mouse *Rplp0* DNA forward qPCR Primer:
ACTGGTCTAGGACCCGAGAAG

Mouse *Rplp0* DNA reverse qPCR Primer:
TCAATGGTGCCTCTGGAGATT

Assessment of cell proliferation rate

The Incucyte® S3 Live-Cell Imaging and Analysis System and its associated software for data processing (Sartorius) were used to assess cell proliferation rate by measuring the increase in confluency over the course of

30 hours. Cells were seeded in 6-well plates at a density of 50,000 cells/cm^2 in triplicates for all experimental conditions and confluency measurements were taken at 0, 6, 12, 18, 24 and 30 hours.

Differentiation of mESCs towards endoderm, mesoderm, and ectoderm lineages

After thawing mESCs, they were passaged twice according to the mESC culture protocol. The day before beginning differentiation protocols, mESCs were passaged using TrypLE™ Express Enzyme 1X (Thermo Fisher, 12604021) supplemented with 10 µM ROCK Inhibitor Y-27632 (STEMCELL Technologies, 72302) for detachment, re-seeding them with a density of 30,000 cells/cm^2 in mESC culture medium in dishes coated with laminin from mouse Engelbreth-Holm-Swarm sarcoma (Roche, 11243217001). For laminin coating, 2.5 µg/cm^2 of laminin diluted in DMEM (Corning, 10-013-CV) was added to cell culture dishes in a minimal volume to coat entire dish surface, after which excess laminin was removed and dishes were air dried for 45 minutes inside sterile cell culture hood. The next day, mESC cultures were rinsed twice with differentiation medium prior to starting differentiation protocols. Differentiations were conducted in triplicates for each experimental condition, maintaining cultures in humidified atmosphere with 5% CO_2 at 37 °C without passaging. Differentiation cultures were rinsed twice daily with differentiation medium prior to adding differentiation treatments to remove dead cells as a fair amount of cell death was expected.

For endoderm differentiation, the differentiation medium consisted of RPMI (Thermo Fisher, 11875093) supplemented with 10% KnockOut™ Serum Replacement (Thermo Fisher, 10828028), 2% B-27™ minus insulin 50X (Thermo Fisher, A1895601), 1.5% HEPES 1M (Thermo Fisher, 15630106), 1% 2-mercaptoethanol 100X (Sigma-Aldrich, ES-007-E), 1% non-essential amino acids 100X (Thermo Fisher, 11140050), 1% L-Glutamine 200 mM (Corning, 25-005-CI), 1% nucleosides 100X (Sigma-Aldrich, ES-008-D) and 1% penicillin-streptomycin 100X (Corning, 30-002-CI). Cells were treated with 5 µM CHIR99021 (Sigma-Aldrich, SML1046) and 50 ng/mL Activin A (R&D Systems, 338-AC) for 1 day followed by 50 ng/mL Activin A (R&D Systems, 338-AC) and 100 nM LDN193189 (STEMCELL Technologies, 72147) for 2 days. Differentiation medium was changed each day, adding freshly prepared treatment mixture.

For mesoderm differentiation, the differentiation medium consisted of EMEM (Corning, 10009CV), 10% KnockOut™ Serum Replacement (Thermo Fisher, 10828028), 1% sodium pyruvate 100 mM (Thermo Fisher, 11360070), 1% 2-mercaptoethanol 100X (Sigma-Aldrich, ES-007-E), 1% non-essential amino acids 100X (Thermo Fisher, 11140050), 1% L-Glutamine 200 mM (Corning, 25-005-CI), 1% nucleosides 100X (Sigma-Aldrich, ES-008-D) and 1% penicillin-streptomycin 100X (Corning, 30-002-CI). Cells were treated with 5 µM CHIR99021 (Sigma-Aldrich, SML1046) and 21 ng/mL BMP-4 (R&D Systems, 5020-BP) for 3 days. Differentiation medium was changed each day, adding freshly prepared treatment mixture.

For ectoderm differentiation, the differentiation medium was the same as the mESC culture medium but without recombinant mouse LIF protein. Cells were treated with 1 µM of retinoic acid (Sigma-Aldrich, R2625) for 3 days. Differentiation medium was changed each day, adding freshly prepared retinoic acid.

On the last day of differentiation protocols, differentiation cultures were sorted based on lineage-specific cell surface and viability markers using fluorescence-activated cell sorting (FACS). Differentiation cultures were rinsed twice with FACS buffer consisting of DPBS 1X (Corning, 21-031-CV) supplemented with 1% ES cell qualified fetal bovine serum (Thermo Fisher, 16141079). A minimal volume of FACS buffer was added to coat entire dish surface and cells were dissociated into single-cell suspension with a cell scraper and gentle pipetting and were transferred to conical tubes. Primary antibodies for cell surface markers were added to cell suspensions in the amount recommended by the manufacturer followed by an incubation of 45 minutes at 4°C, gently mixing every 10 mins. The primary antibodies used for endoderm, mesoderm and ectoderm were anti-CXCR4 (R&D Systems, MAB21651), anti-CDH2 (R&D Systems, AF6426) and anti-NCAM1 (R&D Systems, AF2408), respectively. Cell suspensions were then rinsed twice with FACS buffer and resuspended in FACS buffer containing the fluorophore-

conjugated secondary antibody in the amount recommended by the manufacturer followed by an incubation of 45 minutes at 4°C, gently mixing every 10 mins. The secondary antibodies used for endoderm, mesoderm and ectoderm were APC-conjugated anti-Rat IgG (R&D Systems, F0113), APC-conjugated anti-Sheep IgG (R&D Systems, F0127) and Alexa Fluor™ 488-conjugated anti-Goat IgG (Thermo Fisher, A11055), respectively. Cell suspensions were rinsed twice with FACS buffer and resuspended in FACS buffer at a density of 2M cells/100 µL, transferring them to FACS tubes and adding 5 µL of propidium iodide 10 µg/mL (Thermo Fisher, P1304MP) per sample which was used for assessing viability. Cells were sorted with the BD FACSAria™ Fusion Flow Cytometer (BD Biosciences) and data was processed with the BD FACSDiva™ software v8.0.2. One unstained control sample per differentiation condition and one control sample of dead cells stained with propidium iodide were also sorted. The control sample of dead cells consisted of pooled differentiated cells heated at 65°C for 1 minute in a digital dry bath and then incubated on ice for 1 minute. After sorting, RNA was immediately extracted and stored at -80°C for subsequent mRNA sequencing.

Quantification and statistical analysis

Statistical tests for comparing grouped data were conducted in R v4.3.1 using functions from the stats R core package. To determine whether parametric or non-parametric statistical tests should be used, we first applied the Shapiro-Wilk test for normality using the shapiro.test function as well as Levene's test for homogeneity of variance using the leveneTest function. Parametric testing was conducted if both the Shapiro-Wilk and Levene's tests passed, whereas non-parametric testing was conducted if either one failed. For pairwise comparisons across the three experimental conditions, parametric testing was performed using one-way ANOVA followed by Tukey's HSD test with p-value adjustment via the aov and TukeyHSD functions and non-parametric testing was performed using the Kruskal-Wallis test followed by the Wilcoxon rank-sum test with Benjamini-Hochberg p-value adjustment via the kruskal.test and pairwise.wilcox.test functions. For comparing two groups of data, parametric testing was performed with Student's t test using the t.test function, and non-parametric testing was performed with the Kruskal-Wallis test using the kruskal.test function. Pearson's chi-squared tests were performed with the chisq.test function and principal component analysis with the prcomp function. Differential quantification and statistical analyses of histone-modified regions using MAnorm2 and of gene expression using DESeq2 are described in their respective method details section.

REFERENCES

1. Gibney, E.R., and Nolan, C.M. (2010). Epigenetics and gene expression. Heredity (Edinb) *105*, 4-13. 10.1038/hdy.2010.54.
2. Jenuwein, T., and Allis, C.D. (2001). Translating the histone code. Science *293*, 1074-1080. 10.1126/science.1063127.
3. Breton-Larrivée, M., Elder, E., and McGraw, S. (2019). DNA methylation, environmental exposures and early embryo development. Anim Reprod *16*, 465-474. 10.21451/1984-3143-ar2019-0062.
4. Li, E. (2002). Chromatin modification and epigenetic reprogramming in mammalian development. Nat Rev Genet *3*, 662-673. 10.1038/nrg887.
5. Ohbo, K., and Tomizawa, S. (2015). Epigenetic regulation in stem cell development, cell fate conversion, and reprogramming. Biomol Concepts *6*, 1-9. 10.1515/bmc-2014-0036.
6. Morey, L., Santanach, A., and Di Croce, L. (2015). Pluripotency and Epigenetic Factors in Mouse Embryonic Stem Cell Fate Regulation. Mol Cell Biol *35*, 2716-2728. 10.1128/mcb.00266-15.
7. Vougiouklakis, T., Nakamura, Y., and Saloura, V. (2017). Critical roles of protein methyltransferases and demethylases in the regulation of embryonic stem cell fate. Epigenetics *12*, 1015-1027. 10.1080/15592294.2017.1391430.

8. Shaffer, B., McGraw, S., Xiao, S.C., Chan, D., Trasler, J., and Chaillet, J.R. (2015). The DNMT1 intrinsically disordered domain regulates genomic methylation during development. Genetics *199*, 533-541. 10.1534/genetics.114.173609.
9. Pradhan, S., Bacolla, A., Wells, R.D., and Roberts, R.J. (1999). Recombinant human DNA (cytosine-5) methyltransferase. I. Expression, purification, and comparison of de novo and maintenance methylation. J Biol Chem *274*, 33002-33010. 10.1074/jbc.274.46.33002.
10. Leonhardt, H., Page, A.W., Weier, H.U., and Bestor, T.H. (1992). A targeting sequence directs DNA methyltransferase to sites of DNA replication in mammalian nuclei. Cell *71*, 865-873. 10.1016/0092-8674(92)90561-p.
11. Bashtrykov, P., Jankevicius, G., Smarandache, A., Jurkowska, R.Z., Ragozin, S., and Jeltsch, A. (2012). Specificity of Dnmt1 for methylation of hemimethylated CpG sites resides in its catalytic domain. Chem Biol *19*, 572-578. 10.1016/j.chembiol.2012.03.010.
12. Mortusewicz, O., Schermelleh, L., Walter, J., Cardoso, M.C., and Leonhardt, H. (2005). Recruitment of DNA methyltransferase I to DNA repair sites. Proc Natl Acad Sci U S A *102*, 8905-8909. 10.1073/pnas.0501034102.
13. Li, S.Y., Park, J., Guan, Y., Chung, K., Shrestha, R., Palmer, M.B., and Susztak, K. (2019). DNMT1 in Six2 Progenitor Cells Is Essential for Transposable Element Silencing and Kidney Development. J Am Soc Nephrol *30*, 594-609. 10.1681/asn.2018070687.
14. Davis, K.N., Qu, P.P., Ma, S., Lin, L., Plastini, M., Dahl, N., Plazzi, G., Pizza, F., O'Hara, R., Wong, W.H., et al. (2023). Mutations in human DNA methyltransferase DNMT1 induce specific genome-wide epigenomic and transcriptomic changes in neurodevelopment. Hum Mol Genet *32*, 3105-3120. 10.1093/hmg/ddad123.
15. Li, E., Bestor, T.H., and Jaenisch, R. (1992). Targeted mutation of the DNA methyltransferase gene results in embryonic lethality. Cell *69*, 915-926. 10.1016/0092-8674(92)90611-f.
16. Liao, J., Karnik, R., Gu, H., Ziller, M.J., Clement, K., Tsankov, A.M., Akopian, V., Gifford, C.A., Donaghey, J., Galonska, C., et al. (2015). Targeted disruption of DNMT1, DNMT3A and DNMT3B in human embryonic stem cells. Nat Genet *47*, 469-478. 10.1038/ng.3258.
17. Li, Z., Dai, H., Martos, S.N., Xu, B., Gao, Y., Li, T., Zhu, G., Schones, D.E., and Wang, Z. (2015). Distinct roles of DNMT1-dependent and DNMT1-independent methylation patterns in the genome of mouse embryonic stem cells. Genome Biol *16*, 115. 10.1186/s13059-015-0685-2.
18. Symmank, J., Bayer, C., Schmidt, C., Hahn, A., Pensold, D., and Zimmer-Bensch, G. (2018). DNMT1 modulates interneuron morphology by regulating Pak6 expression through crosstalk with histone modifications. Epigenetics *13*, 536-556. 10.1080/15592294.2018.1475980.
19. Jiang, H., Cao, H.J., Ma, N., Bao, W.D., Wang, J.J., Chen, T.W., Zhang, E.B., Yuan, Y.M., Ni, Q.Z., Zhang, F.K., et al. (2020). Chromatin remodeling factor ARID2 suppresses hepatocellular carcinoma metastasis via DNMT1-Snail axis. Proc Natl Acad Sci U S A *117*, 4770-4780. 10.1073/pnas.1914937117.
20. Merry, C.R., Forrest, M.E., Sabers, J.N., Beard, L., Gao, X.H., Hatzoglou, M., Jackson, M.W., Wang, Z., Markowitz, S.D., and Khalil, A.M. (2015). DNMT1-associated long non-coding RNAs regulate global gene expression and DNA methylation in colon cancer. Hum Mol Genet *24*, 6240-6253. 10.1093/hmg/ddv343.
21. Liu, R., Kim, K.Y., Jung, Y.W., and Park, I.H. (2016). Dnmt1 regulates the myogenic lineage specification of muscle stem cells. Sci Rep *6*, 35355. 10.1038/srep35355.
22. Lee, P.P., Fitzpatrick, D.R., Beard, C., Jessup, H.K., Lehar, S., Makar, K.W., Pérez-Melgosa, M., Sweetser, M.T., Schlissel, M.S., Nguyen, S., et al. (2001). A critical role for Dnmt1 and DNA methylation in T cell development, function, and survival. Immunity *15*, 763-774. 10.1016/s1074-7613(01)00227-8.
23. Londoño Gentile, T., Lu, C., Lodato, P.M., Tse, S., Olejniczak, S.H., Witze, E.S., Thompson, C.B., and Wellen, K.E. (2013). DNMT1 is regulated by ATP-citrate lyase and maintains methylation patterns during adipocyte differentiation. Mol Cell Biol *33*, 3864-3878. 10.1128/mcb.01495-12.
24. Zhang, Y., Chen, F.Q., Sun, Y.H., Zhou, S.Y., Li, T.Y., and Chen, R. (2011). Effects of DNMT1 silencing on malignant phenotype and methylated gene expression in cervical cancer cells. J Exp Clin Cancer Res *30*, 98. 10.1186/1756-9966-30-98.

25. Dagar, V., Hutchison, W., Muscat, A., Krishnan, A., Hoke, D., Buckle, A., Siswara, P., Amor, D.J., Mann, J., Pinner, J., et al. (2018). Genetic variation affecting DNA methylation and the human imprinting disorder, Beckwith-Wiedemann syndrome. Clin Epigenetics *10*, 114. 10.1186/s13148-018-0546-4.
26. Klein, C.J., Botuyan, M.V., Wu, Y., Ward, C.J., Nicholson, G.A., Hammans, S., Hojo, K., Yamanishi, H., Karpf, A.R., Wallace, D.C., et al. (2011). Mutations in DNMT1 cause hereditary sensory neuropathy with dementia and hearing loss. Nat Genet *43*, 595-600. 10.1038/ng.830.
27. Winkelmann, J., Lin, L., Schormair, B., Kornum, B.R., Faraco, J., Plazzi, G., Melberg, A., Cornelio, F., Urban, A.E., Pizza, F., et al. (2012). Mutations in DNMT1 cause autosomal dominant cerebellar ataxia, deafness and narcolepsy. Hum Mol Genet *21*, 2205-2210. 10.1093/hmg/dds035.
28. Hirasawa, R., Chiba, H., Kaneda, M., Tajima, S., Li, E., Jaenisch, R., and Sasaki, H. (2008). Maternal and zygotic Dnmt1 are necessary and sufficient for the maintenance of DNA methylation imprints during preimplantation development. Genes Dev *22*, 1607-1616. 10.1101/gad.1667008.
29. Borowczyk, E., Mohan, K.N., D'Aiuto, L., Cirio, M.C., and Chaillet, J.R. (2009). Identification of a region of the DNMT1 methyltransferase that regulates the maintenance of genomic imprints. Proc Natl Acad Sci U S A *106*, 20806-20811. 10.1073/pnas.0905668106.
30. McGraw, S., Zhang, J.X., Farag, M., Chan, D., Caron, M., Konermann, C., Oakes, C.C., Mohan, K.N., Plass, C., Pastinen, T., et al. (2015). Transient DNMT1 suppression reveals hidden heritable marks in the genome. Nucleic Acids Research *43*, 1485-1497. 10.1093/nar/gku1386.
31. Bartolomei, M.S., and Ferguson-Smith, A.C. (2011). Mammalian genomic imprinting. Cold Spring Harb Perspect Biol *3*. 10.1101/cshperspect.a002592.
32. Li, X., Ito, M., Zhou, F., Youngson, N., Zuo, X., Leder, P., and Ferguson-Smith, A.C. (2008). A maternal-zygotic effect gene, Zfp57, maintains both maternal and paternal imprints. Dev Cell *15*, 547-557. 10.1016/j.devcel.2008.08.014.
33. Quenneville, S., Verde, G., Corsinotti, A., Kapopoulou, A., Jakobsson, J., Offner, S., Baglivo, I., Pedone, P.V., Grimaldi, G., Riccio, A., and Trono, D. (2011). In embryonic stem cells, ZFP57/KAP1 recognize a methylated hexanucleotide to affect chromatin and DNA methylation of imprinting control regions. Mol Cell *44*, 361-372. 10.1016/j.molcel.2011.08.032.
34. Leung, D., Du, T., Wagner, U., Xie, W., Lee, A.Y., Goyal, P., Li, Y., Szulwach, K.E., Jin, P., Lorincz, M.C., and Ren, B. (2014). Regulation of DNA methylation turnover at LTR retrotransposons and imprinted loci by the histone methyltransferase Setdb1. Proc Natl Acad Sci U S A *111*, 6690-6695. 10.1073/pnas.1322273111.
35. Shi, H., Strogantsev, R., Takahashi, N., Kazachenka, A., Lorincz, M.C., Hemberger, M., and Ferguson-Smith, A.C. (2019). ZFP57 regulation of transposable elements and gene expression within and beyond imprinted domains. Epigenetics Chromatin *12*, 49. 10.1186/s13072-019-0295-4.
36. Chiba, H., Hiura, H., Okae, H., Miyauchi, N., Sato, F., Sato, A., and Arima, T. (2013). DNA methylation errors in imprinting disorders and assisted reproductive technology. Pediatr Int *55*, 542-549. 10.1111/ped.12185.
37. Elhamamsy, A.R. (2017). Role of DNA methylation in imprinting disorders: an updated review. J Assist Reprod Genet *34*, 549-562. 10.1007/s10815-017-0895-5.
38. MacDonald, W.A., and Mann, M.R.W. (2014). Epigenetic regulation of genomic imprinting from germ line to preimplantation. Molecular Reproduction and Development *81*, 126-140. https://doi.org/10.1002/mrd.22220.
39. Xie, W., Barr, C.L., Kim, A., Yue, F., Lee, A.Y., Eubanks, J., Dempster, E.L., and Ren, B. (2012). Base-resolution analyses of sequence and parent-of-origin dependent DNA methylation in the mouse genome. Cell *148*, 816-831. 10.1016/j.cell.2011.12.035.
40. Maupetit-Méhouas, S., Montibus, B., Nury, D., Tayama, C., Wassef, M., Kota, S.K., Fogli, A., Cerqueira Campos, F., Hata, K., Feil, R., et al. (2016). Imprinting control regions (ICRs) are marked by mono-allelic bivalent chromatin when transcriptionally inactive. Nucleic Acids Res *44*, 621-635. 10.1093/nar/gkv960.
41. Proudhon, C., Duffié, R., Ajjan, S., Cowley, M., Iranzo, J., Carbajosa, G., Saadeh, H., Holland, M.L., Oakey, R.J., Rakyan, V.K., et al. (2012). Protection against de novo methylation is instrumental in maintaining parent-of-origin methylation inherited from the gametes. Mol Cell *47*, 909-920. 10.1016/j.molcel.2012.07.010.

42. Strogantsev, R., Krueger, F., Yamazawa, K., Shi, H., Gould, P., Goldman-Roberts, M., McEwen, K., Sun, B., Pedersen, R., and Ferguson-Smith, A.C. (2015). Allele-specific binding of ZFP57 in the epigenetic regulation of imprinted and non-imprinted monoallelic expression. Genome Biol *16*, 112. 10.1186/s13059-015-0672-7.
43. Duffié, R., Ajjan, S., Greenberg, M.V., Zamudio, N., Escamilla del Arenal, M., Iranzo, J., Okamoto, I., Barbaux, S., Fauque, P., and Bourc'his, D. (2014). The Gpr1/Zdbf2 locus provides new paradigms for transient and dynamic genomic imprinting in mammals. Genes Dev *28*, 463-478. 10.1101/gad.232058.113.
44. Thorvaldsen, J.L., Mann, M.R., Nwoko, O., Duran, K.L., and Bartolomei, M.S. (2002). Analysis of sequence upstream of the endogenous H19 gene reveals elements both essential and dispensable for imprinting. Mol Cell Biol *22*, 2450-2462. 10.1128/mcb.22.8.2450-2462.2002.
45. Yoon, B.J., Herman, H., Sikora, A., Smith, L.T., Plass, C., and Soloway, P.D. (2002). Regulation of DNA methylation of Rasgrf1. Nat Genet *30*, 92-96. 10.1038/ng795.
46. Lin, S.P., Youngson, N., Takada, S., Seitz, H., Reik, W., Paulsen, M., Cavaille, J., and Ferguson-Smith, A.C. (2003). Asymmetric regulation of imprinting on the maternal and paternal chromosomes at the Dlk1-Gtl2 imprinted cluster on mouse chromosome 12. Nat Genet *35*, 97-102. 10.1038/ng1233.
47. Hiura, H., Sugawara, A., Ogawa, H., John, R.M., Miyauchi, N., Miyanari, Y., Horiike, T., Li, Y., Yaegashi, N., Sasaki, H., et al. (2014). A tripartite paternally methylated region within the Gpr1-Zdbf2 imprinted domain on mouse chromosome 1 identified by meDIP-on-chip. Nucleic Acids Res *42*, 10869. 10.1093/nar/gku624.
48. Wood, A.J., Roberts, R.G., Monk, D., Moore, G.E., Schulz, R., and Oakey, R.J. (2007). A screen for retrotransposed imprinted genes reveals an association between X chromosome homology and maternal germ-line methylation. PLoS Genet *3*, e20. 10.1371/journal.pgen.0030020.
49. Evans, H.K., Weidman, J.R., Cowley, D.O., and Jirtle, R.L. (2005). Comparative Phylogenetic Analysis of Blcap/Nnat Reveals Eutherian-Specific Imprinted Gene. Molecular Biology and Evolution *22*, 1740-1748. 10.1093/molbev/msi165.
50. Williamson, C.M., Turner, M.D., Ball, S.T., Nottingham, W.T., Glenister, P., Fray, M., Tymowska-Lalanne, Z., Plagge, A., Powles-Glover, N., Kelsey, G., et al. (2006). Identification of an imprinting control region affecting the expression of all transcripts in the Gnas cluster. Nature Genetics *38*, 350-355. 10.1038/ng1731.
51. Ono, R., Shiura, H., Aburatani, H., Kohda, T., Kaneko-Ishino, T., and Ishino, F. (2003). Identification of a large novel imprinted gene cluster on mouse proximal chromosome 6. Genome Res *13*, 1696-1705. 10.1101/gr.906803.
52. Lucifero, D., Mertineit, C., Clarke, H.J., Bestor, T.H., and Trasler, J.M. (2002). Methylation dynamics of imprinted genes in mouse germ cells. Genomics *79*, 530-538. 10.1006/geno.2002.6732.
53. Kim, J., Ekram, M.B., Kim, H., Faisal, M., Frey, W.D., Huang, J.M., Tran, K., Kim, M.M., and Yu, S. (2012). Imprinting control region (ICR) of the Peg3 domain. Hum Mol Genet *21*, 2677-2687. 10.1093/hmg/dds092.
54. Yang, T., Adamson, T.E., Resnick, J.L., Leff, S., Wevrick, R., Francke, U., Jenkins, N.A., Copeland, N.G., and Brannan, C.I. (1998). A mouse model for Prader-Willi syndrome imprinting-centre mutations. Nat Genet *19*, 25-31. 10.1038/ng0598-25.
55. Fitzpatrick, G.V., Soloway, P.D., and Higgins, M.J. (2002). Regional loss of imprinting and growth deficiency in mice with a targeted deletion of KvDMR1. Nat Genet *32*, 426-431. 10.1038/ng988.
56. Arima, T., and Wake, N. (2006). Establishment of the primary imprint of the HYMAI/PLAGL1 imprint control region during oogenesis. Cytogenet Genome Res *113*, 247-252. 10.1159/000090839.
57. Zhang, Z., Joh, K., Yatsuki, H., Wang, Y., Arai, Y., Soejima, H., Higashimoto, K., Iwasaka, T., and Mukai, T. (2006). Comparative analyses of genomic imprinting and CpG island-methylation in mouse Murr1 and human MURR1 loci revealed a putative imprinting control region in mice. Gene *366*, 77-86. https://doi.org/10.1016/j.gene.2005.08.020.
58. Shiura, H., Nakamura, K., Hikichi, T., Hino, T., Oda, K., Suzuki-Migishima, R., Kohda, T., Kaneko-Ishino, T., and Ishino, F. (2009). Paternal deletion of Meg1/Grb10 DMR causes maternalization of the Meg1/Grb10 cluster in mouse proximal Chromosome 11 leading to severe pre- and postnatal growth retardation. Human Molecular Genetics *18*, 1424-1438. 10.1093/hmg/ddp049.
59. Wutz, A., Smrzka, O.W., Schweifer, N., Schellander, K., Wagner, E.F., and Barlow, D.P. (1997). Imprinted expression of the Igf2r gene depends on an intronic CpG island. Nature *389*, 745-749. 10.1038/39631.

60. Smith, R.J., Dean, W., Konfortova, G., and Kelsey, G. (2003). Identification of Novel Imprinted Genes in a Genome-Wide Screen for Maternal Methylation. Genome Research *13*, 558-569. 10.1101/gr.781503.
61. Okamura, K., Wintle, R.F., and Scherer, S.W. (2008). Characterization of the differentially methylated region of the Impactgene that exhibits Glires-specific imprinting. Genome Biology *9*, R160. 10.1186/gb-2008-9-11-r160.
62. Song, Q., Decato, B., Hong, E.E., Zhou, M., Fang, F., Qu, J., Garvin, T., Kessler, M., Zhou, J., and Smith, A.D. (2013). A reference methylome database and analysis pipeline to facilitate integrative and comparative epigenomics. PLoS One *8*, e81148. 10.1371/journal.pone.0081148.
63. Wang, L., Zhang, J., Duan, J., Gao, X., Zhu, W., Lu, X., Yang, L., Zhang, J., Li, G., Ci, W., et al. (2014). Programming and inheritance of parental DNA methylomes in mammals. Cell *157*, 979-991. 10.1016/j.cell.2014.04.017.
64. Barral, A., Pozo, G., Ducrot, L., Papadopoulos, G.L., Sauzet, S., Oldfield, A.J., Cavalli, G., and Déjardin, J. (2022). SETDB1/NSD-dependent H3K9me3/H3K36me3 dual heterochromatin maintains gene expression profiles by bookmarking poised enhancers. Mol Cell *82*, 816-832.e812. 10.1016/j.molcel.2021.12.037.
65. Jansz, N. (2019). DNA methylation dynamics at transposable elements in mammals. Essays Biochem *63*, 677-689. 10.1042/ebc20190039.
66. Kigami, D., Minami, N., Takayama, H., and Imai, H. (2003). MuERV-L is one of the earliest transcribed genes in mouse one-cell embryos. Biol Reprod *68*, 651-654. 10.1095/biolreprod.102.007906.
67. Evsikov, A.V., de Vries, W.N., Peaston, A.E., Radford, E.E., Fancher, K.S., Chen, F.H., Blake, J.A., Bult, C.J., Latham, K.E., Solter, D., and Knowles, B.B. (2004). Systems biology of the 2-cell mouse embryo. Cytogenet Genome Res *105*, 240-250. 10.1159/000078195.
68. Peaston, A.E., Evsikov, A.V., Graber, J.H., de Vries, W.N., Holbrook, A.E., Solter, D., and Knowles, B.B. (2004). Retrotransposons regulate host genes in mouse oocytes and preimplantation embryos. Dev Cell *7*, 597-606. 10.1016/j.devcel.2004.09.004.
69. Macfarlan, T.S., Gifford, W.D., Driscoll, S., Lettieri, K., Rowe, H.M., Bonanomi, D., Firth, A., Singer, O., Trono, D., and Pfaff, S.L. (2012). Embryonic stem cell potency fluctuates with endogenous retrovirus activity. Nature *487*, 57-63. 10.1038/nature11244.
70. Eckersley-Maslin, M.A., Svensson, V., Krueger, C., Stubbs, T.M., Giehr, P., Krueger, F., Miragaia, R.J., Kyriakopoulos, C., Berrens, R.V., Milagre, I., et al. (2016). MERVL/Zscan4 Network Activation Results in Transient Genome-wide DNA Demethylation of mESCs. Cell Rep *17*, 179-192. 10.1016/j.celrep.2016.08.087.
71. Zalzman, M., Falco, G., Sharova, L.V., Nishiyama, A., Thomas, M., Lee, S.-L., Stagg, C.A., Hoang, H.G., Yang, H.-T., Indig, F.E., et al. (2010). Zscan4 regulates telomere elongation and genomic stability in ES cells. Nature *464*, 858-863. 10.1038/nature08882.
72. Zhang, Q., Dan, J., Wang, H., Guo, R., Mao, J., Fu, H., Wei, X., and Liu, L. (2016). Tcstv1 and Tcstv3 elongate telomeres of mouse ES cells. Scientific Reports *6*, 19852. 10.1038/srep19852.
73. Raefski, A.S., and O'Neill, M.J. (2005). Identification of a cluster of X-linked imprinted genes in mice. Nat Genet *37*, 620-624. 10.1038/ng1567.
74. Ben-Porath, I., Thomson, M.W., Carey, V.J., Ge, R., Bell, G.W., Regev, A., and Weinberg, R.A. (2008). An embryonic stem cell-like gene expression signature in poorly differentiated aggressive human tumors. Nat Genet *40*, 499-507. 10.1038/ng.127.
75. Foster, C.T., Dovey, O.M., Lezina, L., Luo, J.L., Gant, T.W., Barlev, N., Bradley, A., and Cowley, S.M. (2010). Lysine-specific demethylase 1 regulates the embryonic transcriptome and CoREST stability. Mol Cell Biol *30*, 4851-4863. 10.1128/mcb.00521-10.
76. Macrae, T.A., Fothergill-Robinson, J., and Ramalho-Santos, M. (2023). Regulation, functions and transmission of bivalent chromatin during mammalian development. Nat Rev Mol Cell Biol *24*, 6-26. 10.1038/s41580-022-00518-2.
77. Müller, F.J., Laurent, L.C., Kostka, D., Ulitsky, I., Williams, R., Lu, C., Park, I.H., Rao, M.S., Shamir, R., Schwartz, P.H., et al. (2008). Regulatory networks define phenotypic classes of human stem cell lines. Nature *455*, 401-405. 10.1038/nature07213.

78. Wong, D.J., Liu, H., Ridky, T.W., Cassarino, D., Segal, E., and Chang, H.Y. (2008). Module map of stem cell genes guides creation of epithelial cancer stem cells. Cell Stem Cell *2*, 333-344. 10.1016/j.stem.2008.02.009.
79. Liberzon, A., Birger, C., Thorvaldsdóttir, H., Ghandi, M., Mesirov, J.P., and Tamayo, P. (2015). The Molecular Signatures Database (MSigDB) hallmark gene set collection. Cell Syst *1*, 417-425. 10.1016/j.cels.2015.12.004.
80. Pujana, M.A., Han, J.D., Starita, L.M., Stevens, K.N., Tewari, M., Ahn, J.S., Rennert, G., Moreno, V., Kirchhoff, T., Gold, B., et al. (2007). Network modeling links breast cancer susceptibility and centrosome dysfunction. Nat Genet *39*, 1338-1349. 10.1038/ng.2007.2.
81. Leonard, M.O., Cottell, D.C., Godson, C., Brady, H.R., and Taylor, C.T. (2003). The role of HIF-1 alpha in transcriptional regulation of the proximal tubular epithelial cell response to hypoxia. J Biol Chem *278*, 40296-40304. 10.1074/jbc.M302560200.
82. Mense, S.M., Sengupta, A., Zhou, M., Lan, C., Bentsman, G., Volsky, D.J., and Zhang, L. (2006). Gene expression profiling reveals the profound upregulation of hypoxia-responsive genes in primary human astrocytes. Physiol Genomics *25*, 435-449. 10.1152/physiolgenomics.00315.2005.
83. Elvidge, G.P., Glenny, L., Appelhoff, R.J., Ratcliffe, P.J., Ragoussis, J., and Gleadle, J.M. (2006). Concordant regulation of gene expression by hypoxia and 2-oxoglutarate-dependent dioxygenase inhibition: the role of HIF-1alpha, HIF-2alpha, and other pathways. J Biol Chem *281*, 15215-15226. 10.1074/jbc.M511408200.
84. Winter, S.C., Buffa, F.M., Silva, P., Miller, C., Valentine, H.R., Turley, H., Shah, K.A., Cox, G.J., Corbridge, R.J., Homer, J.J., et al. (2007). Relation of a hypoxia metagene derived from head and neck cancer to prognosis of multiple cancers. Cancer Res *67*, 3441-3449. 10.1158/0008-5472.Can-06-3322.
85. Qi, J., Nakayama, K., Cardiff, R.D., Borowsky, A.D., Kaul, K., Williams, R., Krajewski, S., Mercola, D., Carpenter, P.M., Bowtell, D., and Ronai, Z.A. (2010). Siah2-dependent concerted activity of HIF and FoxA2 regulates formation of neuroendocrine phenotype and neuroendocrine prostate tumors. Cancer Cell *18*, 23-38. 10.1016/j.ccr.2010.05.024.
86. Yang, H., Bai, D., Li, Y., Yu, Z., Wang, C., Sheng, Y., Liu, W., Gao, S., and Zhang, Y. (2022). Allele-specific H3K9me3 and DNA methylation co-marked CpG-rich regions serve as potential imprinting control regions in pre-implantation embryo. Nature Cell Biology *24*, 783-792. 10.1038/s41556-022-00900-4.
87. Tort, F., Ferrer-Cortès, X., Thió, M., Navarro-Sastre, A., Matalonga, L., Quintana, E., Bujan, N., Arias, A., García-Villoria, J., Acquaviva, C., et al. (2014). Mutations in the lipoyltransferase LIPT1 gene cause a fatal disease associated with a specific lipoylation defect of the 2-ketoacid dehydrogenase complexes. Hum Mol Genet *23*, 1907-1915. 10.1093/hmg/ddt585.
88. Soreze, Y., Boutron, A., Habarou, F., Barnerias, C., Nonnenmacher, L., Delpech, H., Mamoune, A., Chrétien, D., Hubert, L., Bole-Feysot, C., et al. (2013). Mutations in human lipoyltransferase gene LIPT1 cause a Leigh disease with secondary deficiency for pyruvate and alpha-ketoglutarate dehydrogenase. Orphanet J Rare Dis *8*, 192. 10.1186/1750-1172-8-192.
89. Taché, V., Bivina, L., White, S., Gregg, J., Deignan, J., Boyadjievd, S.A., and Poulain, F.R. (2016). Lipoyltransferase 1 Gene Defect Resulting in Fatal Lactic Acidosis in Two Siblings. Case Rep Obstet Gynecol *2016*, 6520148. 10.1155/2016/6520148.
90. Ni, M., Solmonson, A., Pan, C., Yang, C., Li, D., Notzon, A., Cai, L., Guevara, G., Zacharias, L.G., Faubert, B., et al. (2019). Functional Assessment of Lipoyltransferase-1 Deficiency in Cells, Mice, and Humans. Cell Rep *27*, 1376-1386.e1376. 10.1016/j.celrep.2019.04.005.
91. Motta, M., Fasano, G., Gredy, S., Brinkmann, J., Bonnard, A.A., Simsek-Kiper, P.O., Gulec, E.Y., Essaddam, L., Utine, G.E., Guarnetti Prandi, I., et al. (2021). SPRED2 loss-of-function causes a recessive Noonan syndrome-like phenotype. Am J Hum Genet *108*, 2112-2129. 10.1016/j.ajhg.2021.09.007.
92. Abshagen, K., Berger, C., Dietrich, A., Schütz, T., Wittekind, C., Stumvoll, M., Blüher, M., and Klöting, N. (2020). A Human REPIN1 Gene Variant: Genetic Risk Factor for the Development of Nonalcoholic Fatty Liver Disease. Clin Transl Gastroenterol *11*, e00114. 10.14309/ctg.0000000000000114.
93. Lai, W., Wu, Y., Sha, L., Lai, Q., Yang, X., Ai, F., Zhang, Q., Bu, F., He, S., Zhu, X., and Chen, L. (2024). Identifying Genetic Factors of Polycystic Ovary Syndrome in Women with Epilepsy: A Whole-Genome Sequencing Study. Neuroendocrinology *114*, 223-233. 10.1159/000534531.

94. Dibbens, L.M., Reid, C.A., Hodgson, B., Thomas, E.A., Phillips, A.M., Gazina, E., Cromer, B.A., Clarke, A.L., Baram, T.Z., Scheffer, I.E., et al. (2010). Augmented currents of an HCN2 variant in patients with febrile seizure syndromes. Ann Neurol *67*, 542-546. 10.1002/ana.21909.
95. DiFrancesco, J.C., Barbuti, A., Milanesi, R., Coco, S., Bucchi, A., Bottelli, G., Ferrarese, C., Franceschetti, S., Terragni, B., Baruscotti, M., and DiFrancesco, D. (2011). Recessive loss-of-function mutation in the pacemaker HCN2 channel causing increased neuronal excitability in a patient with idiopathic generalized epilepsy. J Neurosci *31*, 17327-17337. 10.1523/jneurosci.3727-11.2011.
96. Nakamura, Y., Shi, X., Numata, T., Mori, Y., Inoue, R., Lossin, C., Baram, T.Z., and Hirose, S. (2013). Novel HCN2 mutation contributes to febrile seizures by shifting the channel's kinetics in a temperature-dependent manner. PLoS One *8*, e80376. 10.1371/journal.pone.0080376.
97. Li, M., Maljevic, S., Phillips, A.M., Petrovski, S., Hildebrand, M.S., Burgess, R., Mount, T., Zara, F., Striano, P., Schubert, J., et al. (2018). Gain-of-function HCN2 variants in genetic epilepsy. Hum Mutat *39*, 202-209. 10.1002/humu.23357.
98. Margolin, D.H., Kousi, M., Chan, Y.M., Lim, E.T., Schmahmann, J.D., Hadjivassiliou, M., Hall, J.E., Adam, I., Dwyer, A., Plummer, L., et al. (2013). Ataxia, dementia, and hypogonadotropism caused by disordered ubiquitination. N Engl J Med *368*, 1992-2003. 10.1056/NEJMoa1215993.
99. Santens, P., Van Damme, T., Steyaert, W., Willaert, A., Sablonnière, B., De Paepe, A., Coucke, P.J., and Dermaut, B. (2015). RNF216 mutations as a novel cause of autosomal recessive Huntington-like disorder. Neurology *84*, 1760-1766. 10.1212/wnl.0000000000001521.
100. Esteves, E., Mendes, V.M., Manadas, B., Lopes, R., Bernardino, L., Correia, M.J., Barros, M., Esteves, A.C., and Rosa, N. (2022). COVID-19 Salivary Protein Profile: Unravelling Molecular Aspects of SARS-CoV-2 Infection. J Clin Med *11*. 10.3390/jcm11195571.
101. Verona, R.I., Thorvaldsen, J.L., Reese, K.J., and Bartolomei, M.S. (2008). The transcriptional status but not the imprinting control region determines allele-specific histone modifications at the imprinted H19 locus. Mol Cell Biol *28*, 71-82. 10.1128/mcb.01534-07.
102. Sanz, L.A., Chamberlain, S., Sabourin, J.C., Henckel, A., Magnuson, T., Hugnot, J.P., Feil, R., and Arnaud, P. (2008). A mono-allelic bivalent chromatin domain controls tissue-specific imprinting at Grb10. Embo j *27*, 2523-2532. 10.1038/emboj.2008.142.
103. Wang, M., Chen, Z., and Zhang, Y. (2022). CBP/p300 and HDAC activities regulate H3K27 acetylation dynamics and zygotic genome activation in mouse preimplantation embryos. Embo j *41*, e112012. 10.15252/embj.2022112012.
104. Voigt, P., LeRoy, G., Drury, W.J., 3rd, Zee, B.M., Son, J., Beck, D.B., Young, N.L., Garcia, B.A., and Reinberg, D. (2012). Asymmetrically modified nucleosomes. Cell *151*, 181-193. 10.1016/j.cell.2012.09.002.
105. Duncan, I.W. (2002). Transvection Effects in Drosophila. Annual Review of Genetics *36*, 521-556. https://doi.org/10.1146/annurev.genet.36.060402.100441.
106. Tartof, K.D., and Henikoff, S. (1991). Trans-sensing effects from Drosophila to humans. Cell *65*, 201-203. 10.1016/0092-8674(91)90153-p.
107. Rassoulzadegan, M., Magliano, M., and Cuzin, F. (2002). Transvection effects involving DNA methylation during meiosis in the mouse. Embo j *21*, 440-450. 10.1093/emboj/21.3.440.
108. Liu, H., Huang, J., Wang, J., Jiang, S., Bailey, A.S., Goldman, D.C., Welcker, M., Bedell, V., Slovak, M.L., Clurman, B., et al. (2008). Transvection mediated by the translocated cyclin D1 locus in mantle cell lymphoma. J Exp Med *205*, 1843-1858. 10.1084/jem.20072102.
109. Creyghton, M.P., Cheng, A.W., Welstead, G.G., Kooistra, T., Carey, B.W., Steine, E.J., Hanna, J., Lodato, M.A., Frampton, G.M., Sharp, P.A., et al. (2010). Histone H3K27ac separates active from poised enhancers and predicts developmental state. Proc Natl Acad Sci U S A *107*, 21931-21936. 10.1073/pnas.1016071107.
110. Kubo, N., Chen, P.B., Hu, R., Ye, Z., Sasaki, H., and Ren, B. (2024). H3K4me1 facilitates promoter-enhancer interactions and gene activation during embryonic stem cell differentiation. Mol Cell. 10.1016/j.molcel.2024.02.030.

111. Rada-Iglesias, A., Bajpai, R., Swigut, T., Brugmann, S.A., Flynn, R.A., and Wysocka, J. (2011). A unique chromatin signature uncovers early developmental enhancers in humans. Nature *470*, 279-283. 10.1038/nature09692.
112. Shlyueva, D., Stampfel, G., and Stark, A. (2014). Transcriptional enhancers: from properties to genome-wide predictions. Nature Reviews Genetics *15*, 272-286. 10.1038/nrg3682.
113. Chuang, L.S., Ian, H.I., Koh, T.W., Ng, H.H., Xu, G., and Li, B.F. (1997). Human DNA-(cytosine-5) methyltransferase-PCNA complex as a target for p21WAF1. Science *277*, 1996-2000. 10.1126/science.277.5334.1996.
114. Iida, T., Suetake, I., Tajima, S., Morioka, H., Ohta, S., Obuse, C., and Tsurimoto, T. (2002). PCNA clamp facilitates action of DNA cytosine methyltransferase 1 on hemimethylated DNA. Genes Cells *7*, 997-1007. 10.1046/j.1365-2443.2002.00584.x.
115. Davies, C., Brown, C.M., Westphal, D., Ward, J.M., and Ward, V.K. (2015). Murine norovirus replication induces G0/G1 cell cycle arrest in asynchronously growing cells. J Virol *89*, 6057-6066. 10.1128/jvi.03673-14.
116. Li, X., Lin, F., Wu, Y., Liu, N., Wang, J., Chen, R., and Lu, Z. (2019). Resveratrol attenuates inflammation environment-induced nucleus pulposus cell senescence in vitro. Biosci Rep *39*. 10.1042/bsr20190126.
117. Barra, V., Schillaci, T., Lentini, L., Costa, G., and Di Leonardo, A. (2012). Bypass of cell cycle arrest induced by transient DNMT1 post-transcriptional silencing triggers aneuploidy in human cells. Cell Div *7*, 2. 10.1186/1747-1028-7-2.
118. Sasatani, M., Xu, Y., Kawai, H., Cao, L., Tateishi, S., Shimura, T., Li, J., Iizuka, D., Noda, A., Hamasaki, K., et al. (2015). RAD18 activates the G2/M checkpoint through DNA damage signaling to maintain genome integrity after ionizing radiation exposure. PLoS One *10*, e0117845. 10.1371/journal.pone.0117845.
119. Selvarajah, J., Elia, A., Carroll, V.A., and Moumen, A. (2015). DNA damage-induced S and G2/M cell cycle arrest requires mTORC2-dependent regulation of Chk1. Oncotarget *6*, 427-440. 10.18632/oncotarget.2813.
120. Meyerson, M., and Harlow, E. (1994). Identification of G1 kinase activity for cdk6, a novel cyclin D partner. Mol Cell Biol *14*, 2077-2086. 10.1128/mcb.14.3.2077-2086.1994.
121. Lundberg, A.S., and Weinberg, R.A. (1998). Functional inactivation of the retinoblastoma protein requires sequential modification by at least two distinct cyclin-cdk complexes. Mol Cell Biol *18*, 753-761. 10.1128/mcb.18.2.753.
122. Wang, Z., Xie, Y., Zhang, L., Zhang, H., An, X., Wang, T., and Meng, A. (2008). Migratory localization of cyclin D2-Cdk4 complex suggests a spatial regulation of the G1-S transition. Cell Struct Funct *33*, 171-183. 10.1247/csf.08019.
123. Ando, K., Ajchenbaum-Cymbalista, F., and Griffin, J.D. (1993). Regulation of G1/S transition by cyclins D2 and D3 in hematopoietic cells. Proc Natl Acad Sci U S A *90*, 9571-9575. 10.1073/pnas.90.20.9571.
124. Bennin, D.A., Don, A.S., Brake, T., McKenzie, J.L., Rosenbaum, H., Ortiz, L., DePaoli-Roach, A.A., and Horne, M.C. (2002). Cyclin G2 associates with protein phosphatase 2A catalytic and regulatory B' subunits in active complexes and induces nuclear aberrations and a G1/S phase cell cycle arrest. J Biol Chem *277*, 27449-27467. 10.1074/jbc.M111693200.
125. Arachchige Don, A.S., Dallapiazza, R.F., Bennin, D.A., Brake, T., Cowan, C.E., and Horne, M.C. (2006). Cyclin G2 is a centrosome-associated nucleocytoplasmic shuttling protein that influences microtubule stability and induces a p53-dependent cell cycle arrest. Exp Cell Res *312*, 4181-4204. 10.1016/j.yexcr.2006.09.023.
126. Le, X.F., Arachchige-Don, A.S., Mao, W., Horne, M.C., and Bast, R.C., Jr. (2007). Roles of human epidermal growth factor receptor 2, c-jun NH2-terminal kinase, phosphoinositide 3-kinase, and p70 S6 kinase pathways in regulation of cyclin G2 expression in human breast cancer cells. Mol Cancer Ther *6*, 2843-2857. 10.1158/1535-7163.Mct-07-0109.
127. Zimmermann, M., Arachchige-Don, A.S., Donaldson, M.S., Dallapiazza, R.F., Cowan, C.E., and Horne, M.C. (2012). Elevated cyclin G2 expression intersects with DNA damage checkpoint signaling and is required for a potent G2/M checkpoint arrest response to doxorubicin. J Biol Chem *287*, 22838-22853. 10.1074/jbc.M112.376855.

128. de Lange, T. (1998). Telomeres and senescence: ending the debate. Science *279*, 334-335. 10.1126/science.279.5349.334.
129. Bodnar, A.G., Ouellette, M., Frolkis, M., Holt, S.E., Chiu, C.P., Morin, G.B., Harley, C.B., Shay, J.W., Lichtsteiner, S., and Wright, W.E. (1998). Extension of life-span by introduction of telomerase into normal human cells. Science *279*, 349-352. 10.1126/science.279.5349.349.
130. Rubio, M.A., Kim, S.H., and Campisi, J. (2002). Reversible manipulation of telomerase expression and telomere length. Implications for the ionizing radiation response and replicative senescence of human cells. J Biol Chem *277*, 28609-28617. 10.1074/jbc.M203747200.
131. Holz-Schietinger, C., and Reich, N.O. (2010). The inherent processivity of the human de novo methyltransferase 3A (DNMT3A) is enhanced by DNMT3L. J Biol Chem *285*, 29091-29100. 10.1074/jbc.M110.142513.
132. Veland, N., Lu, Y., Hardikar, S., Gaddis, S., Zeng, Y., Liu, B., Estecio, M.R., Takata, Y., Lin, K., Tomida, M.W., et al. (2019). DNMT3L facilitates DNA methylation partly by maintaining DNMT3A stability in mouse embryonic stem cells. Nucleic Acids Res *47*, 152-167. 10.1093/nar/gky947.
133. Okano, M., Bell, D.W., Haber, D.A., and Li, E. (1999). DNA methyltransferases Dnmt3a and Dnmt3b are essential for de novo methylation and mammalian development. Cell *99*, 247-257. 10.1016/s0092-8674(00)81656-6.
134. Kuroda, T., Yasuda, S., Tachi, S., Matsuyama, S., Kusakawa, S., Tano, K., Miura, T., Matsuyama, A., and Sato, Y. (2019). SALL3 expression balance underlies lineage biases in human induced pluripotent stem cell differentiation. Nature Communications *10*, 2175. 10.1038/s41467-019-09511-4.
135. Yan, R., Cheng, X., Gu, C., Xu, Y., Long, X., Zhai, J., Sun, F., Qian, J., Du, Y., Wang, H., and Guo, F. (2023). Dynamics of DNA hydroxymethylation and methylation during mouse embryonic and germline development. Nature Genetics *55*, 130-143. 10.1038/s41588-022-01258-x.
136. Saxena, S., Maroju, P.A., Choudhury, S., Anne, A., and Mohan, K.N. (2020). Analysis of transcript levels of a few schizophrenia candidate genes in neurons from a transgenic mouse embryonic stem cell model overexpressing DNMT1. Gene *757*, 144934. https://doi.org/10.1016/j.gene.2020.144934.
137. D'Aiuto, L., Di Maio, R., Mohan, K.N., Minervini, C., Saporiti, F., Soreca, I., Greenamyre, J.T., and Chaillet, J.R. (2011). Mouse ES cells overexpressing DNMT1 produce abnormal neurons with upregulated NMDA/NR1 subunit. Differentiation *82*, 9-17. https://doi.org/10.1016/j.diff.2011.03.003.
138. Patel, K., Dickson, J., Din, S., Macleod, K., Jodrell, D., and Ramsahoye, B. (2010). Targeting of 5-aza-2'-deoxycytidine residues by chromatin-associated DNMT1 induces proteasomal degradation of the free enzyme. Nucleic Acids Res *38*, 4313-4324. 10.1093/nar/gkq187.
139. Pappalardi, M.B., Keenan, K., Cockerill, M., Kellner, W.A., Stowell, A., Sherk, C., Wong, K., Pathuri, S., Briand, J., Steidel, M., et al. (2021). Discovery of a first-in-class reversible DNMT1-selective inhibitor with improved tolerability and efficacy in acute myeloid leukemia. Nat Cancer *2*, 1002-1017.
140. Azevedo Portilho, N., Saini, D., Hossain, I., Sirois, J., Moraes, C., and Pastor, W.A. (2021). The DNMT1 inhibitor GSK-3484862 mediates global demethylation in murine embryonic stem cells. Epigenetics & Chromatin *14*, 56. 10.1186/s13072-021-00429-0.
141. Lai, Q., Xu, Y.H., Chen, Q., Tang, L., Li, A.G., Zhang, L.F., Zhang, C.F., Song, J.F., and Du, Z.Z. (2017). The loss-of-function of DNA methyltransferase 1 by siRNA impairs the growth of non-small cell lung cancer with alleviated side effects via reactivation of RASSF1A and APC in vitro and vivo. Oncotarget *8*, 59301-59311. 10.18632/oncotarget.19573.
142. Karolchik, D., Hinrichs, A.S., Furey, T.S., Roskin, K.M., Sugnet, C.W., Haussler, D., and Kent, W.J. (2004). The UCSC Table Browser data retrieval tool. Nucleic Acids Res *32*, D493-496. 10.1093/nar/gkh103.
143. Liao, Y., Smyth, G.K., and Shi, W. (2019). The R package Rsubread is easier, faster, cheaper and better for alignment and quantification of RNA sequencing reads. Nucleic Acids Research *47*, e47-e47. 10.1093/nar/gkz114.
144. Cavalcante, R.G., and Sartor, M.A. (2017). annotatr: genomic regions in context. Bioinformatics *33*, 2381-2383. 10.1093/bioinformatics/btx183.

145. Abascal, F., Acosta, R., Addleman, N.J., Adrian, J., Afzal, V., Ai, R., Aken, B., Akiyama, J.A., Jammal, O.A., Amrhein, H., et al. (2020). Expanded encyclopaedias of DNA elements in the human and mouse genomes. Nature *583*, 699-710. 10.1038/s41586-020-2493-4.
146. Bourgey, M., Dali, R., Eveleigh, R., Chen, K.C., Letourneau, L., Fillon, J., Michaud, M., Caron, M., Sandoval, J., Lefebvre, F., et al. (2019). GenPipes: an open-source framework for distributed and scalable genomic analyses. GigaScience *8*. 10.1093/gigascience/giz037.
147. Bolger, A.M., Lohse, M., and Usadel, B. (2014). Trimmomatic: a flexible trimmer for Illumina sequence data. Bioinformatics *30*, 2114-2120. 10.1093/bioinformatics/btu170.
148. Krueger, F., and Andrews, S.R. (2011). Bismark: a flexible aligner and methylation caller for Bisulfite-Seq applications. Bioinformatics *27*, 1571-1572. 10.1093/bioinformatics/btr167.
149. Tarasov, A., Vilella, A.J., Cuppen, E., Nijman, I.J., and Prins, P. (2015). Sambamba: fast processing of NGS alignment formats. Bioinformatics *31*, 2032-2034. 10.1093/bioinformatics/btv098.
150. Li, H., and Durbin, R. (2009). Fast and accurate short read alignment with Burrows–Wheeler transform. Bioinformatics *25*, 1754-1760. 10.1093/bioinformatics/btp324.
151. Li, H., Handsaker, B., Wysoker, A., Fennell, T., Ruan, J., Homer, N., Marth, G., Abecasis, G., and Durbin, R. (2009). The Sequence Alignment/Map format and SAMtools. Bioinformatics *25*, 2078-2079. 10.1093/bioinformatics/btp352.
152. Zhang, Y., Liu, T., Meyer, C.A., Eeckhoute, J., Johnson, D.S., Bernstein, B.E., Nusbaum, C., Myers, R.M., Brown, M., Li, W., and Liu, X.S. (2008). Model-based Analysis of ChIP-Seq (MACS). Genome Biology *9*, R137. 10.1186/gb-2008-9-9-r137.
153. Quinlan, A.R., and Hall, I.M. (2010). BEDTools: a flexible suite of utilities for comparing genomic features. Bioinformatics *26*, 841-842. 10.1093/bioinformatics/btq033.
154. Tu, S., Li, M., Chen, H., Tan, F., Xu, J., Waxman, D.J., Zhang, Y., and Shao, Z. (2021). MAnorm2 for quantitatively comparing groups of ChIP-seq samples. Genome Res *31*, 131-145. 10.1101/gr.262675.120.
155. Gu, Z., Eils, R., and Schlesner, M. (2016). Complex heatmaps reveal patterns and correlations in multidimensional genomic data. Bioinformatics *32*, 2847-2849. 10.1093/bioinformatics/btw313.
156. Gu, Z., Eils, R., Schlesner, M., and Ishaque, N. (2018). EnrichedHeatmap: an R/Bioconductor package for comprehensive visualization of genomic signal associations. BMC Genomics *19*, 234. 10.1186/s12864-018-4625-x.
157. Zheng, R., Wan, C., Mei, S., Qin, Q., Wu, Q., Sun, H., Chen, C.-H., Brown, M., Zhang, X., Meyer, C.A., and Liu, X S. (2018). Cistrome Data Browser: expanded datasets and new tools for gene regulatory analysis. Nucleic Acids Research *47*, D729-D735. 10.1093/nar/gky1094.
158. Takahashi, N., Coluccio, A., Thorball, C.W., Planet, E., Shi, H., Offner, S., Turelli, P., Imbeault, M., Ferguson-Smith, A.C., and Trono, D. (2019). ZNF445 is a primary regulator of genomic imprinting. Genes Dev *33*, 49-54. 10.1101/gad.320069.118.
159. Fornes, O., Castro-Mondragon, J.A., Khan, A., van der Lee, R., Zhang, X., Richmond, P.A., Modi, B.P., Correard, S., Gheorghe, M., Baranašić, D., et al. (2020). JASPAR 2020: update of the open-access database of transcription factor binding profiles. Nucleic Acids Res *48*, D87-d92. 10.1093/nar/gkz1001.
160. Bailey, T.L., Johnson, J., Grant, C.E., and Noble, W.S. (2015). The MEME Suite. Nucleic Acids Research *43*, W39-W49. 10.1093/nar/gkv416.
161. Dobin, A., Davis, C.A., Schlesinger, F., Drenkow, J., Zaleski, C., Jha, S., Batut, P., Chaisson, M., and Gingeras, T.R. (2013). STAR: ultrafast universal RNA-seq aligner. Bioinformatics *29*, 15-21. 10.1093/bioinformatics/bts635.
162. Anders, S., Pyl, P.T., and Huber, W. (2015). HTSeq--a Python framework to work with high-throughput sequencing data. Bioinformatics *31*, 166-169. 10.1093/bioinformatics/btu638.
163. Pertea, M., Pertea, G.M., Antonescu, C.M., Chang, T.-C., Mendell, J.T., and Salzberg, S.L. (2015). StringTie enables improved reconstruction of a transcriptome from RNA-seq reads. Nature Biotechnology *33*, 290-295. 10.1038/nbt.3122.
164. Love, M.I., Huber, W., and Anders, S. (2014). Moderated estimation of fold change and dispersion for RNA-seq data with DESeq2. Genome Biology *15*, 550. 10.1186/s13059-014-0550-8.

165. Liao, Y., Smyth, G.K., and Shi, W. (2014). featureCounts: an efficient general purpose program for assigning sequence reads to genomic features. Bioinformatics *30*, 923-930. 10.1093/bioinformatics/btt656.
166. Liao, Y., Smyth, G.K., and Shi, W. (2013). The Subread aligner: fast, accurate and scalable read mapping by seed-and-vote. Nucleic Acids Research *41*, e108-e108. 10.1093/nar/gkt214.
167. Wu, T., Hu, E., Xu, S., Chen, M., Guo, P., Dai, Z., Feng, T., Zhou, L., Tang, W., Zhan, L., et al. (2021). clusterProfiler 4.0: A universal enrichment tool for interpreting omics data. Innovation (Camb) *2*, 100141. 10.1016/j.xinn.2021.100141.
168. Subramanian, A., Tamayo, P., Mootha, V.K., Mukherjee, S., Ebert, B.L., Gillette, M.A., Paulovich, A., Pomeroy, S.L., Golub, T.R., Lander, E.S., and Mesirov, J.P. (2005). Gene set enrichment analysis: A knowledge-based approach for interpreting genome-wide expression profiles. Proceedings of the National Academy of Sciences *102*, 15545-15550. doi:10.1073/pnas.0506580102.
169. Hahne, F., and Ivanek, R. (2016). Visualizing Genomic Data Using Gviz and Bioconductor. In Statistical Genomics: Methods and Protocols, E. Mathé, and S. Davis, eds. (Springer New York), pp. 335-351. 10.1007/978-1-4939-3578-9_16.
170. Ramírez, F., Ryan, D.P., Grüning, B., Bhardwaj, V., Kilpert, F., Richter, A.S., Heyne, S., Dündar, F., and Manke, T. (2016). deepTools2: a next generation web server for deep-sequencing data analysis. Nucleic Acids Research *44*, W160-W165. 10.1093/nar/gkw257.
171. Edgar, R., Domrachev, M., and Lash, A.E. (2002). Gene Expression Omnibus: NCBI gene expression and hybridization array data repository. Nucleic Acids Res *30*, 207-210. 10.1093/nar/30.1.207.
172. Barrett, T., Wilhite, S.E., Ledoux, P., Evangelista, C., Kim, I.F., Tomashevsky, M., Marshall, K.A., Phillippy, K.H., Sherman, P.M., Holko, M., et al. (2013). NCBI GEO: archive for functional genomics data sets--update. Nucleic Acids Res *41*, D991-995. 10.1093/nar/gks1193.
173. Callicott, R.J., and Womack, J.E. (2006). Real-time PCR assay for measurement of mouse telomeres. Comp Med *56*, 17-22.
174. Cawthon, R.M. (2002). Telomere measurement by quantitative PCR. Nucleic Acids Res *30*, e47. 10.1093/nar/30.10.e47.
175. Livak, K.J., and Schmittgen, T.D. (2001). Analysis of relative gene expression data using real-time quantitative PCR and the 2(-Delta Delta C(T)) Method. Methods *25*, 402-408. 10.1006/meth.2001.1262.